ISSN 0016-7037
Volume 75, Number 1
January 1, 2011

ELSEVIER

Geochimica et Cosmochimica Acta

JOURNAL OF THE GEOCHEMICAL SOCIETY AND THE METEORITICAL SOCIETY

Volume 75, Number 1 January 1, 2011

Articles

Continued on outside back cover

(This is a sample cover image for this issue. The actual cover is not yet available at this time.)

Available online at www.sciencedirect.com

SciVerse ScienceDirect

Geochimica et Cosmochimica Acta 75 (2011) 6300–6329

Geochimica et Cosmochimica Acta

www.elsevier.com/locate/gca

Understanding melt generation beneath the slow-spreading Kolbeinsey Ridge using ^{238}U, ^{230}Th, and ^{231}Pa excesses

L.J. Elkins [a,b,*], K.W.W. Sims [a,c], J. Prytulak [d,e], T. Elliott [e,g], N. Mattielli [f,g], J. Blichert-Toft [h], J. Blusztajn [a], N. Dunbar [i], C. Devey [j], D.F. Mertz [k], J.-G. Schilling [l], M. Murrell [m]

[a] *Woods Hole Oceanographic Institution, Woods Hole, MA, USA*
[b] *Dept. of Geology, Bryn Mawr College, Bryn Mawr, PA, USA*
[c] *Dept. of Geology and Geophysics, University of Wyoming, Laramie, WY, USA*
[d] *Oxford University, Oxford, UK*
[e] *Bristol Isotope Group, School of Earth Sciences, University of Bristol, Bristol, UK*
[f] *Université de Bruxelles, Brussels, Belgium*
[g] *Faculteit der Aardwetenschappen, de Boelelaan 1085, 1081HV Amsterdam, Netherlands*
[h] *Laboratoire de Géologie de Lyon, Ecole Normale Supérieure de Lyon and Université Claude Bernard Lyon 1, CNRS UMR 5276, 46 Allée d'Italie, 69007 Lyon, France*
[i] *New Mexico Institute of Mining and Technology, Socorro, NM, USA*
[j] *IFM-GEOMAR, Wischhofstr. 1-3, D-24148 Kiel, Germany*
[k] *Institute of Geosciences, University of Mainz, 55099 Mainz, Germany*
[l] *Univ. Rhode Island, Narragansett, RI, USA*
[m] *Los Alamos National Laboratory, Los Alamos, NM, USA*

Received 18 August 2010; accepted in revised form 9 August 2011

Abstract

To examine the petrogenesis and sources of basalts from the Kolbeinsey Ridge, one of the shallowest locations along the global ridge system, we present new measurements of Nd, Sr, Hf, and Pb isotopes and U-series disequilibria on 32 axial basalts. Young Kolbeinsey basalts (full-spreading rate = 1.8 cm/yr; 67°05′–70°26′N) display $(^{230}Th/^{238}U) < 1$ and $(^{230}Th/^{238}U) > 1$ with $(^{230}Th/^{238}U)$ from 0.95 to 1.30 and have low U (11.3–65.6 ppb) and Th (33.0 ppb–2.40 ppm) concentrations. Except for characteristic isotopic enrichment near the Jan Mayen region, the otherwise depleted Kolbeinsey basalts (e.g. $^{87}Sr/^{86}Sr = 0.70272$–$0.70301$, $\varepsilon_{Nd} = 8.4$–10.5, $\varepsilon_{Hf} = 15.4$–19.6 $(La/Yb)_N = 0.28$–0.84) encompass a narrow range of $(^{230}Th/^{232}Th)$ (1.20–1.32) over a large range in $(^{238}U/^{232}Th)$ (0.94–1.32), producing a horizontal array on a $(^{230}Th/^{232}Th)$ vs. $(^{238}U/^{232}Th)$ diagram and a large variation in $(^{230}Th/^{238}U)$. However, the $(^{230}Th/^{238}U)$ of the Kolbeinsey Ridge basalts (0.96–1.30) are inversely correlated with $(^{234}U/^{238}U)$ (1.001–1.031). Samples with low $(^{230}Th/^{238}U)$ and elevated $(^{234}U/^{238}U)$ reflect alteration by seawater or seawater-derived materials. The unaltered Kolbeinsey lavas with equilibrium $^{234}U/^{238}U$ have high $(^{230}Th/^{238}U)$ values ($\geqslant 1.2$), which are consistent with melting in the presence of garnet. This is in keeping with the thick crust and anomalously shallow axial depth for the Kolbeinsey Ridge, which is thought to be the product of large degrees of melting in a long melt column. A time-dependent, dynamic melting scenario involving a long, slowly upwelling melting column that initiates well within the garnet peridotite stability zone can, in general, reproduce the $(^{230}Th/^{238}U)$ and $(^{231}Pa/^{235}U)$ ratios in uncontaminated Kolbeinsey lavas, but low $(^{231}Pa/^{235}U)$ ratios in Eggvin Bank samples suggest eclogite involvement in the source for that ridge segment.

* Corresponding author at: Dept. of Geology, Bryn Mawr College, Bryn Mawr, PA 19010, USA.
E-mail address: lelkins@brynmawr.edu (L.J. Elkins).

0016-7037/$ - see front matter © 2011 Elsevier Ltd. All rights reserved.
doi:10.1016/j.gca.2011.08.020

1. INTRODUCTION

Mid-ocean ridge basalt (MORB) chemistry varies systematically as a function of ridge depth, which was posited to be related to underlying crustal thickness (Klein and Langmuir, 1987). Deep mid-ocean ridges overlie relatively thin ocean crust and are inferred to be produced by shallow, small degree melting in relatively short mantle melt columns; whereas shallow mid-ocean ridges overlie thick crust and are inferred to be produced by large degrees of melting in long melting columns with deep initiation of melting.

Among global mid-ocean systems, the slow-spreading Kolbeinsey Ridge (~1.8 cm/yr; Mosar et al., 2002) north of Iceland represents Klein and Langmuir's (1987) shallow end member, due to its shallow ridge axis (mean depth ~1100 m). Relative to other MORB, the Kolbeinsey Ridge erupts basalts that are highly depleted in trace elements and have both low Na_8, suggesting large degrees of melting, and high Fe_8, suggesting deep initiation of melting (Klein and Langmuir, 1987).

Using a limited global data set, and following on the model of Klein and Langmuir (1987), Bourdon et al. (1996a) predicted that production of thick crust at shallow mid-ocean ridges, such as the Kolbeinsey Ridge, involves a long, deep melt column initiating in the garnet peridotite stability field, thus producing large melt fractions with high ($^{230}Th/^{238}U$) ratios. However, since there have been no published U-series measurements for the Kolbeinsey Ridge, these predictions rely on extrapolation and have yet to be verified.

The Klein and Langmuir (1987) model provides a general, first-order perspective on MORB petrogenesis. However, since this early model was introduced, MORB chemistry has proven to be much more diverse than originally thought, and other factors besides melt column length have been shown to play an important role in MORB compositions. For example, mantle lithology, variations in mineral/melt partition coefficients, mantle potential temperature (e.g. the effect of the Iceland hot spot) and melting at multiple porosities are thought to be some of the controlling parameters establishing the chemical composition of MORB (e.g. Langmuir et al., 1992; Niu and Batiza, 1993, 1997; Lundstrom et al., 1995; Sims et al., 1995, 2002; Lundstrom, 2000; Niu et al., 2001; Donnelly et al., 2004; Stracke et al., 2006; Russo et al., 2009; Waters et al., 2011). As will be discussed in detail below, an important aspect of Kolbeinsey Ridge basalts is that they are all highly depleted with relatively uniform major and trace element compositions and Nd, Sr, Hf, and Pb isotopic abundances, except near Jan Mayen and Iceland. This uniformity suggests that for our sample suite, the petrogenetic processes are remarkably similar and that the source is homogeneous over the length scale of melting. This is in marked contrast to locations such as the East Pacific Rise (EPR) where considerable variability is observed over small spatial and temporal scales and indicates melting of mixed lithologies (Donnelly et al., 2004; Waters et al., 2011).

It is important to note that Kolbeinsey Ridge basalts variably record the effects of crustal contamination (Michael and Cornell, 1998). Michael and Cornell (1998) measured Cl/K ratios in Kolbeinsey MORB that range up to 0.54, which they interpreted as representing variable assimilation of hydrothermally altered crustal material in shallow crystallizing magma. They hypothesized that at slow-spreading ridges with thick crust, such as the Kolbeinsey Ridge, magmas can pool in the crust and experience more hydrothermal and shallow crustal alteration than they do in comparable locations with thin crust. Such alteration with seawater components can have a significant impact on the U-series systematics of MORB (Bourdon et al., 2000; Sims et al., 2003; Breivik et al., 2009; Fjeldskaar et al., 2009).

In this contribution we present measurements of ^{238}U–^{230}Th–^{226}Ra and ^{235}U–^{231}Pa isotopes, Sr, Nd, Hf, and Pb isotopic compositions, and major and trace element abundances from the Kolbeinsey Ridge. We first consider the effects of seawater alteration by measuring ($^{234}U/^{238}U$) and Cl/K_2O ratios, both sensitive tracers of basalt alteration in the crust. We find a systematic correlation between ($^{234}U/^{238}U$) and ($^{230}Th/^{238}U$), which enables correction of the ($^{230}Th/^{238}U$) ratios to unaltered values (i.e. ($^{234}U/^{238}U$) = 1.000). The corrected values for Kolbeinsey Ridge lavas closely resemble the Th isotopic ratios and extent of ^{238}U–^{230}Th disequilibria measured in unaltered samples. After deciphering and then filtering for secondary effects, we use the combined U-series, long-lived isotopic, and trace element measurements to test the hypothesis that global axial ridge depth is strongly controlled by mantle temperature effects on solidus depth and melt supply, as opposed to alternatives such as mantle source heterogeneity. Namely, because the Kolbeinsey Ridge basalts have shallow eruption depths, they should result from large extents of melting in a long melt column initiating well within the garnet stability field. We develop a self-consistent forward melting model that can account for the combined U-series isotopes and major and trace element compositions, thereby providing a more comprehensive understanding of the parameters controlling basalt petrogenesis at this slow spreading ridge (e.g. solidus depths, upwelling rates, melt porosities, melt extraction mechanisms, and variations in source composition).

2. BACKGROUND

2.1. Geological setting

The Kolbeinsey Ridge is a shallow, slow-spreading ridge (~1.8 cm/yr; Mosar et al., 2002) extending northwards from Iceland at 66.5°N to the Jan Mayen Fracture Zone at 71°N (Fig. 1 and Table 1). Given the high sedimentation rate of the North Atlantic, particularly in near-coastal areas and during periods of deglaciation, any dredged fresh glasses from the Kolbeinsey Ridge axis should reflect active rifting and eruption in the last few thousand years (Devey et al., 1994; Haase et al., 2003).

The ridge is offset from the northeast Iceland volcanic province by the Tjörnes Fracture Zone, from which the southern Kolbeinsey segment extends northward to the Spar Fracture Zone at 69°N, and the northern segment

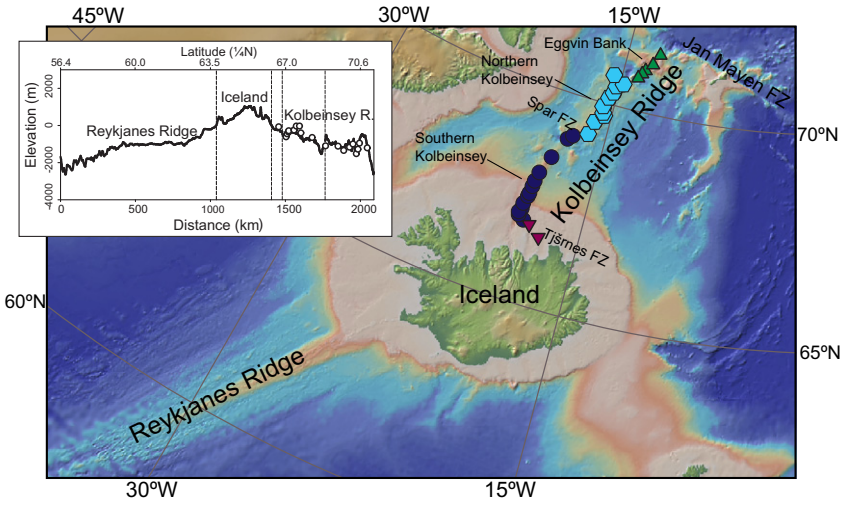

Fig. 1. Map of field area. The geographic coverage of the sample suite analyzed in this study, shown as data points, encompasses the entire Kolbeinsey Ridge. Inset: depth profile for the Reykjanes Ridge, Iceland, and the Kolbeinsey Ridge, with Kolbeinsey Ridge sample locations as open circles. Bathymetry from Smith and Sandwell (1997) and Jakobsson et al. (2008).

extends from the Spar Fracture Zone to the Jan Mayen Fracture Zone. An additional, small overlapping spreading center at 70.7°N (Haase et al., 2003) delineates the small Eggvin Bank ridge segment (Brandsdottir et al., 2004; Hooft et al., 2006). The ridge averages 1100 m depth overall and deepens northward from Iceland (~200 m) until it reaches its maximum depth (~1500 m) at 69°N, just south of the Spar Fracture Zone. The central ridge shallows northward towards the Eggvin Bank, which is in places only 40 m below sea level (Fig. 1, inset). Seismic studies (Kodaira et al., 1997; Mjelde et al., 2008) have shown that the Kolbeinsey Ridge crustal section is 7–10 km thick. This physical characteristic contrasts with the global average oceanic crustal thickness of 6–7 km (Mjelde et al., 2009).

2.2. Geologic age constraints

During the last glacial period (terminating around 10,000 yr BP in the North Atlantic; e.g. Bauch et al., 2001, and references therein; Knudsen et al., 2004), Iceland and shallow parts of the Kolbeinsey Ridge were subaerial and glaciated. Extensive outwash during subsequent deglaciation covered the ocean floor with a thick veneer of glacial debris, which thickens towards Iceland. In areas with volcanic morphological features visible in bathymetric profiles, some sampling efforts have only retrieved sediment and ice-rafted glacial debris, suggesting the volcanic features in those areas predate glaciation (Baumann et al., 1993; Lackschewitz et al., 1994; Hooft et al., 2006). Measured sediment thicknesses in pull-apart basins along the Tjörnes FZ range from at least 100 m for the small Grimsey Graben (Montesi and Behn, 2007) to up to 4 km in the 700 m deep Eyjafjarðarall basin, the southernmost expression of the Kolbeinsey Ridge (Hooft et al., 2006). Post-glacial volcanism (<10 ka) along the length of the ridge axis has erupted through or onto this outwash. High-resolution multi-beam bathymetry of the Tjörnes FZ and Southern Kolbeinsey Ridge (Brandsdottir et al., 2004; Hooft et al., 2006) shows glacial sediment covering the ocean floor and a well-developed neovolcanic zone in the center of the ridge. This geological relationship suggests that any glass recovered from the neovolcanic zone is expected to be <10 ka, which is an essential constraint when interpreting ^{238}U–^{230}Th and ^{235}U–^{231}Pa disequilibria.

2.3. Chemical and isotopic compositions

Many of the samples analyzed here for U-series disequilibria have been previously characterized for their long-lived radiogenic Sr, Nd, Hf, and Pb isotopic compositions, in addition to major and trace element abundances, including isotope dilution measurements of Rb, Sr, Sm, Nd, U, Th, Pb, Lu, and Hf (Sigurdsson, 1981; Schilling et al., 1983; Neumann and Schilling, 1984; Michael et al., 1989; Waggoner, 1989; Mertz et al., 1991; Devey et al., 1994; Michael, 1995; Mertz and Haase, 1997; Schilling et al., 1999; Hanan et al., 2000; Haase et al., 2003; Andres et al., 2004; Blichert-Toft et al., 2005). The Kolbeinsey Ridge basalts investigated in this study are olivine tholeiites (MgO = 6–10 wt.%; Devey et al., 1994). Fractionation-corrected Na_2O (Na_8) and FeO (Fe_8) contents in the lavas are among the lowest and highest, respectively, found on the global ridge system, suggesting they are the result of a deep (high Fe_8) onset of large degrees of melting (low Na_8; Klein and Langmuir, 1987). Compared to most other MORB, Kolbeinsey basalts are depleted in trace elements (e.g. average $(La/Yb)_N = 0.41$, whereas N–MORB from the East Pacific Rise have average $(La/Yb)_N$ of 0.72 (Sims et al., 2002) and global N–MORB ratios average 0.67 (Hofmann, 1988)). Mertz et al. (1991) and Mertz and Haase (1997) demonstrated small but systematic variations in $^{87}Sr/^{86}Sr$ and ε_{Nd} along the Kolbeinsey Ridge (e.g. $^{87}Sr/^{86}Sr$ = 0.7027–0.7030), with increasingly radiogenic $^{87}Sr/^{86}Sr$ towards Iceland. Mertz et al. (1991) also observed that the most radiogenic samples have the most depleted trace element signatures. They argued, based on uniform

Table 1
List of samples measured for this study, with initial and final dredge locations, cruise legs, and brief sample descriptions from cruise reports where available.

Sample	Location	Cruise	Year	Start Latitude (°N)[a]	End Latitude (°N)	Start Longitude (°N)	End Longitude (°N)	Start Depth (m)	End Depth (m)	Description
TRI0139-001-001G	Tjörnes FZ	R/V Trident 139	1971	66.5100	66.5100	−17.3400	−17.3400	72	72	Fresh basalt glass
POS185 1105B	Tjörnes FZ	R.V. Poseidon 185	1991	66.7527	66.7527	−18.0910	−18.0910	397	467	Vesicular, numerous small plag. phenocrysts, glass
POS185 1093	S. Kolbeinsey	R.V. Poseidon 185	1991	66.8386	66.8386	−18.7070	−18.7070	610	580	Glass
POS291 485-3	S. Kolbeinsey	R.V. Poseidon 291	2002	66.8987	66.8955	−18.7480	−18.7455	460	451	5 × 5 × 5 cm, fresh basalt with glass
TRI0139-007-001G	S. Kolbeinsey	R/V Trident 139	1971	66.9100	66.9100	−18.7700	−18.7700	405	405	Fresh basalt glass
POS326 540DS-4	S. Kolbeinsey	R.V. Poseidon 326	2005	66.9567	66.9667	−18.4077	−18.4062	131	186	Lava fragment 8 × 6 × 4 cm, glass crust up to 1.5 cm, no alteration, porphyric, plag. <21% up to 0.2 cm, vesicles 30% 0.1–1 cm
POS291 495-2	S. Kolbeinsey	R.V. Poseidon 291	2002	66.9842	66.9842	−18.7320	−18.7225	384	333	8 × 8 × 5 cm, fresh basalt with glass
POS185 1096A	S. Kolbeinsey	R.V. Poseidon 185	1991	66.9990	66.9990	−18.7040	−18.7040	346	298	Glassy basalt, small vesicles
POS185 1094B	S. Kolbeinsey	R.V. Poseidon 185	1991	67.0000	67.0000	−18.6645	−18.6645	285	270	Glass
TRI0139-006-002G	S. Kolbeinsey	R/V Trident 139	1971	67.0100	67.0100	−18.7100	−18.7100	290	290	Fresh basalt glass
TRI0139-013-001G	S. Kolbeinsey	R/V Trident 139	1971	67.3100	67.3100	−18.6600	−18.6600	250	250	Fresh basalt glass
TRI0139-013-003G	S. Kolbeinsey	R/V Trident 139	1971	67.3100	67.3100	−18.6600	−18.6600	250	250	Fresh basalt glass
POS229 304DS	S. Kolbeinsey	R.V. Poseidon 229	1997	67.4398	67.4414	−18.5727	−18.5517	307	323	Sheet flow, 10–15 mm glassy rim, 10% plag.-phenos (1mm), organic material
TRI0139-014-001G	S. Kolbeinsey	R/V Trident 139	1971	67.4800	67.4800	−18.6300	−18.6300	390	390	Fresh basalt glass
POS 229 270DS	S. Kolbeinsey	R.V. Poseidon 229	1997	67.6275	67.6323	−18.5345	−18.5228	320	325	Pillow sector, 5 mm glass rim, aphyric, few vesicles
TRI0139-015-001G	S. Kolbeinsey	R/V Trident 139	1971	67.7100	67.7100	−18.5400	−18.5400	402	402	Fresh basalt glass
TRI0139-016-001G	S. Kolbeinsey	R/V Trident 139	1971	67.9000	67.9000	−18.4100	−18.4100	565	565	Fresh basalt glass
POS0002/2 Geo 212[a]	S. Kolbeinsey	Polarstern ARK V/Ib	1988	67.9250	67.9250	−18.3623	−18.3623			Non-consolidated hyaloclastite
TRI0139-020-001G	S. Kolbeinsey	R/V Trident 139	1971	68.3700	68.3700	−17.9900	−17.9900	675	650	Fresh basalt glass
POS221 596DS-1	S. Kolbeinsey	R.V. Poseidon 221	1996	68.8715	68.8773	−17.3625	−17.3667	1350	1300	Pillow, 5 mm glass, vesicles, rare 1 mm plag. phenocrysts
POS221 605DS-2	S. Kolbeinsey	R.V. Poseidon 221	1996	68.9985	68.9850	−17.0768	−17.0470	1500	1750	Pillow, 1 cm glass, 2–5 mm vesicles, rare plag. phenocrysts
POS210/1 682DS-1	N. Kolbeinsey	R.V. Poseidon 210/1	1995	69.1392	69.1473	−16.1813	−16.1787	1100	1170	Basalt, glass rim <0.5 cm, few vesicles <2 mm, aphyric
POLARK7-1-21844	N. Kolbeinsey	Polarstern ARK VII/I	1990	69.4650	69.4650	−15.9903	−15.9903	1226	1226	None available
POLARK7-1-21847	N. Kolbeinsey	Polarstern ARK VII/I	1990	69.6597	69.6597	−15.5388	−15.5388	983	983	None available
POLARK7-1-21848	N. Kolbeinsey	Polarstern ARK VII/I	1990	69.8088	69.8088	−15.7008	−15.7008	1116	1116	None available
POLARK7-1-21850	N. Kolbeinsey	Polarstern ARK VII/I	1990	70.1180	70.1180	−15.2967	−15.2967	1346	1346	None available
POLARK7-1-21854	N. Kolbeinsey	Polarstern ARK VII/I	1990	70.4432	70.4432	−14.8063	−14.8063	1169	1169	None available
POLARK7-1-21856-3	N. Kolbeinsey	Polarstern ARK VII/I	1990	70.6238	70.6238	−15.5263	−15.5263	1001	1001	None available
POS210/1 700DS-2	Eggvin Bank	R.V. Poseidon 210/1	1995	70.8482	70.8475	−13.6415	−13.6617	1280	1350	Homogeneous basalt, thick glass rim, many big vesicles (~1 cm), aphyric

POS210/1 702DS-1	Eggvin Bank	R.V. Poseidon 210/1	1995	70.7740	70.7725	−13.5778	−13.5832	1520	1550	Pillow, homogeneous, grey basalt, thick glass rim, vesicles (~1 mm and more)
POS210/1 698DS-1	Eggvin Bank	R.V. Poseidon 210/1	1995	71.0615	71.0577	−13.1138	−13.1260	645	650	Sheet flow fragment, fresh glass rim, >5% vesicles (1 mm), ~5% plag. phenocrysts (<0.5 cm), <1% ol. phenocrysts (<3mm)
TRI0139-027-005G	Eggvin Bank	R/V Trident 139	1971	71.3300	71.3300	−12.6400	−12.6400	1205	1205	Fresh basalt glass

Sample POS0002/2 Geo 212 recovered by box corer in 1988 (Mertz et al., 1991); no depths were recorded for this sample. All other samples recovered by dredging.
[a] Start and end positions for dredges are not available for older cruises, due to the high uncertainties in determining ship position at that time. More accurate positions are available for the newer cruises listed.

$^{206}Pb/^{204}Pb$ isotope ratios, which contrast with Icelandic basalts, that the Iceland plume component is not involved in Kolbeinsey Ridge magmatism. In contrast, Schilling et al. (1999) documented gradients in He, Pb, Sr, and Nd isotopes and trace element characteristics (e.g. Th/U) across the Tjörnes FZ and southern Kolbeinsey Ridge that they interpreted as mapping the northward dispersion of the Iceland plume. Blichert-Toft et al. (2005) conducted principal component analysis of relatively small but significant $^{206}Pb/^{204}Pb$, $^{207}Pb/^{204}Pb$, and $^{208}Pb/^{204}Pb$ variations along the Kolbeinsey Ridge and suggested that the lavas formed as a result of mixing between a "FOZO"-like component (Hart et al., 1992) and a "depleted MORB mantle" (DMM) component (Blichert-Toft et al., 2005).

Kolbeinsey Ridge MORB from the Eggvin Bank ridge segment, north of ~70.7°N, have more enriched radiogenic isotopic compositions than their southern counterparts (Schilling et al., 1999; Tronnes et al., 1999; Haase et al., 2003; Mertz et al., 2004; Blichert-Toft et al., 2005), with the most locally isotopically enriched values on the Jan Mayen rise (where "more enriched" refers to long-term incompatible element enrichment as manifested through more radiogenic $^{87}Sr/^{86}Sr$, $^{206}Pb/^{204}Pb$, $^{207}Pb/^{204}Pb$, and $^{208}Pb/^{204}Pb$ ratios, and less radiogenic ε_{Nd} and ε_{Hf} values). Schilling et al. (1999) and Neumann and Schilling (1984) suggested that the isotope signatures are the result of a laterally dispersing mantle plume beneath the Jan Mayen region, while others have suggested cool edge effects or trapped subcontinental material in the mantle beneath Jan Mayen (Tronnes et al., 1999; Mertz et al., 2004; Debaille et al., 2009).

3. ANALYTICAL METHODS

3.1. ^{238}U–^{230}Th–^{226}Ra and ^{235}U–^{231}Pa analyses

All samples analyzed in this study were hand-picked, visibly fresh glasses that were previously lightly leached (a 15-min leach with ultrasonication in ultrapure 0.1 N hydrochloric acid with 2% hydrogen peroxide, followed by a 15-min leach with ultrasonication in ultrapure 0.1 N oxalic acid with 2% hydrogen peroxide) and rinsed in high-purity distilled water to remove surface impurities. The samples were subsequently hand-picked a second time and even sometimes a third time to ensure high quality of the glass. Both careful hand-picking and light leaching has been shown to be essential for removing surficial coatings on submarine samples (e.g. Verma, 1992; Bourdon et al., 2000), if samples have been crustally contaminated or surficially altered, the U-series nuclides can and will be perturbed as shown by this work and other published studies (e.g. Aumento, 1971; Turekian and Bertine, 1971; Störzer and Selo, 1976, 1978; Macdougall, 1977; Bacon, 1978; Macdougall et al., 1979; Bourdon et al., 2000; Sims et al., 2002, 2003, 2006; Glass et al., 2005; Pelt et al., 2008; Pietruszka et al., 2009, 2011).

Uranium-series isotopes were measured by multi-collector inductively-coupled plasma mass spectrometry (MC–ICP-MS) at the Woods Hole Oceanographic Institution (WHOI) (methods outlined in Sims et al. (2008a,b) and Ball

Table 2
Measured U, Th, and Pa isotopic data from the Kolbeinsey Ridge.

Sample	Th (ppm)	U (ppm)	Pa (fg/g)	(^{230}Th)/(^{238}U)[f]	±[g] (%)	(^{238}U)/(^{232}Th)	± (%)	(^{230}Th)/(^{232}Th)	± (%)	(^{234}U)/(^{238}U)[j]	± (%)	(^{231}Pa)/(^{235}U)[h]	± (%)	(^{230}Th)/(^{238}U)$_c$[l]	(^{231}Pa)/(^{235}U)$_{max}$[k]	± (%)
Samples measured																
TRI0139-001-001G[a]	0.0345	0.0113	–	–		–		–		**1.001**	**0.3**	–				
POS185 1105B[b]	0.0328	0.0138	–	0.997	2.1	1.274	1.9	1.270	2.0	1.020	0.1	–		1.186		
POS185 1093[a]	0.110	0.0339	27.7	1.285	2.0	0.935	2.2	1.202	2.0	**1.000**	**0.2**	2.50	0.8	1.273	2.85	0.8
TRI0139-007-001G[a]	–	0.0506	–	–		–		–		1.010	0.2	–				
(replicate)[a]	0.152	0.0512	36.3	1.224	1.3	1.026	1.5	1.255	1.3	1.013	0.2	2.18	0.7			
Average	0.152	0.0509	36.3			1.026	1.5	1.3	1.3	1.012		2.2	0.7	1.323		
POS326 540DS-4[b]	0.0748	0.0319	–	0.988	2.0	1.292	1.9	1.276	0.5	1.031	0.2	–		1.280		
POS291 495-2[b]	0.136	0.0449	–	1.209	2.2	1.002	2.1	1.212	0.3	**1.002**	**0.1**	–		1.228		
POS185 1096A[b]	0.161	0.0525	–	1.253	1.9	0.992	1.9	1.242	0.2	**1.004**	**0.1**	–		1.294		
POS185 1094B[b]	0.103	0.0340	–	1.197	2.0	0.999	2.0	1.196	0.4	**1.003**	**0.1**	–		1.230		
TRI0139-006-002G[a]	–	0.0416	–	–		–		–		1.003	0.2	–				
(replicate)[a]	0.129	0.0420	32.6	1.259	3.7	0.986	3.7	1.242	3.5	1.010	0.2	2.39	0.5			
(replicate)[b]	0.124	0.0407	–	1.221	2.2	0.995	2.2	1.216	0.3	1.009	0.1	–				
Average	0.127	0.0414	32.6			0.991	4.3	1.229	3.5	1.008	0.2	2.39	0.5	1.307		
TRI0139-013-003G[b]	0.102	0.0347	–	1.223	2.5	1.033	2.5	1.263	0.2	**1.005**	**0.1**	–		1.268		
POS 229 304DS[c]	0.111	0.0403	–	1.172	2.8	1.103	2.0	1.293	2.0	–		–				
TRI0139-014-001G[b]	0.176	0.0679	–	1.070	1.9	1.170	1.9	1.251	0.2	1.028	0.2	–		1.334		
POS 229 270DS[c]	0.126	0.0431	–	1.239	2.8	1.038	2.0	1.287	2.0	–		–				
TRI0139-015-001G[a]	0.0937	0.0303	24.7	1.287	2.3	0.980	2.7	1.261	2.4	1.005	0.2	2.48	0.8			
(replicate)[a]	–	0.0305	–	–		–		–		1.003	0.2	–				
(replicate)[b]	0.0915	0.0311	–	1.098	2.5	1.032	0.02	1.133	1.6	1.007	0.1	–				
Average	0.0926	0.0306	24.7			1.006		1.197		**1.005**		2.48	0.8	1.214	2.83	0.8
TRI0139-016-001G[b]	0.118	0.0391	–	1.228	1.9	1.001	1.9	1.228	0.2	1.010	0.1	–		1.317		
POS0002/2 Geo 212[b]	0.114	0.0387	–	1.216	1.9	1.032	1.9	1.255	0.2	1.006	0.1	–		1.271		
TRI0139-020-001G[a]	–	0.0865	–	–		–		–		1.004	0.2	–				
(replicate)[a]	0.249	0.0861	64.0	1.265	1.1	1.047	1.2	1.324	1.1	1.006	0.2	2.26	0.6			
Average	0.249	0.0863	64.0			1.047	1.2	1.324	1.1	**1.005**	**0.3**	2.26	0.6	1.305	2.56	0.7
POS221 596DS-1[b]	0.207	0.0704	–	1.190	2.2	1.031	2.2	1.226	0.2	1.009	0.1	–		1.275		
POS221 605DS-2[b]	0.208	0.0735	–	1.168	2.0	1.073	2.0	1.253	0.3	1.013	0.1	–		1.290		
POS210/1 682DS-1[b]	0.107	0.0361	–	1.296	1.9	1.022	0.02	1.324	0.02	**1.002**	**0.2**	–		1.312		
POLARK7-1-21844[b]	0.0464	0.0175	–	0.978	2.0	1.146	1.9	1.121	2.0	1.018	0.2	–		1.149		
POLARK7-1-21847[b]	0.0336	0.0127	–	–		1.151	2.0	–		–		–				
(replicate)[a]	–	0.0128	13.0	–		–		–		1.017	0.3	3.10	1.3			
(replicate)[a]	0.0336	0.0128	–	1.059	3.4	1.156	3.5	1.224	3.5	1.015	0.3	–				
Average	0.0336	0.0128	13.022			1.154	4.0	1.224	3.5	1.016	0.4	3.10	1.3	1.150		
POLARK7-1-21848[d]	0.0752	0.0280	–	1.121	2.8	1.129	2.0	1.265	2.0	–		–				
POLARK7-1-21850[d]	0.0766	0.0250	–	1.261	2.8	0.988	2.0	1.247	2.0	–		–				
POLARK7-1-21854[d]	0.0615	0.0261	–	0.965	2.8	1.287	2.0	1.242	2.0	–		–				
POS210/1 702 DS-1[b,i]	0.358	0.104	–	1.235	2.2	0.883	2.2	1.090	0.2	**1.003**	**0.1**	–		1.267		

POS210/1 700 DS-2[a]	0.847	0.225	–	1.192	0.5	0.806	0.6	0.961	0.5	1.003	0.2	–		1.186		
(replicate)[a]	–	0.224	90.1	–		–		–		1.002	0.2	1.22	0.6			
(replicate)[a]	0.852	0.226	–	1.186	0.8	0.803	0.8	0.953	0.7	0.997	0.2	–				
Average	0.850	0.225	90.1			0.804	1.1	0.957	0.8	**1.001**	**0.3**	1.22	0.6		1.27	0.7
POS210/1 698 DS-1[a]	0.915	0.242	–	1.214	0.5	0.803	0.6	0.975	0.5	1.007	0.2	–		1.275		
TRI0139-027-005G [b]	2.398	0.656	–	1.179	1.9	0.830	1.9	0.979	0.2	**1.004**	**0.1**	–		1.219		
Standards measured as unknowns[e]																
ATh-O 09/06[b]	7.532	2.351	–	1.075	2.1	0.947	2.1	1.018	0.1	1.006	0.05	–				
ATh-O 10/07[b]	7.385	2.302	–	1.076	2.5	0.946	2.5	1.017	0.1	1.002	0.1	–				
BHVO-1 09/06[b]	1.207	0.4344	–	0.991	1.9	1.092	1.9	1.081	0.1	1.003	0.1	–				
W-2 09/06[b]	2.157	0.5101	–	0.983	1.9	0.717	1.9	0.705	0.1	1.005	0.1	–				
BCR-1 03/08[b]	5.665	1.683	–	0.981	2.0	0.901	2.0	0.884	0.1	1.004	0.1	–				
TML 03/08[b]	29.789	10.505	–	1.000	2.1	1.070	2.1	1.070	0.1	1.003	0.04	–				
BCR-2 Average[a]	5.835	1.670	–			0.874	1.0	0.872	1.1	1.003	0.41	1.00	1.3			
TML Average[a]	29.705	10.481	–			0.935	0.4	1.070	0.8	1.000	0.78	–				

[a] U, Th, and/or Pa concentrations and isotopes measured by MC–ICP-MS (ThermoFinnigan Neptune) at the University of Bristol, Bristol, UK. Th concentration and isotopic data are not presented for one sample batch for which Th was not successfully extracted; analyses of affected samples were replicated on a second sample dissolution. Th isotopic data are not presented for sample TRI0139-001-001G due to analytical difficulty arising from its low Th concentrations and small sample size.

[b] U, Th, and/or Ra concentrations and isotopes measured by ICP-MS (isotope concentrations and ratios measured using ThermoFinnigan Element2 and Neptune, respectively) at the Woods Hole Oceanographic Inst. (WHOI), Woods Hole, MA.

[c] Sample analyzed for U and Th concentrations and isotopes by TIMS at Amsterdam.

[d] Sample analyzed for U and Th concentrations and isotopes by TIMS at Los Alamos National Laboratory (LANL), Los Alamos, NM.

[e] Each line of data represents analysis for a single dissolution and extraction, consisting of ICP-MS or MC–ICP-MS sample blocks of 20+ analyses. Standard measurements reported in data table represent individual ICP-MS runs of standards that were dissolved, extracted, and analyzed alongside Kolbeinsey Ridge samples as unknowns; these runs are independent of routine analyses of standards for accuracy calibration purposes, the results of which are presented in Sims et al. (2008a) and summarized in the text. Results for standard analyses at Bristol were previously reported in Prytulak et al. (2008), and here we present averages for those results with 2σ standard deviations.

[f] Data are reported using the following decay constant values: $\lambda_{U\text{-}238} = 1.551 \times 10^{-10}$ (Jaffey et al., 1971), $\lambda_{Th\text{-}232} = 4.948 \times 10^{-11}$ (Le Roux and Glendenin, 1963), $\lambda_{Th\text{-}230} = 9.158 \times 10^{-6}$ (Cheng et al., 2000), $\lambda_{U\text{-}234} = 2.826 \times 10^{-6}$ (Cheng et al., 2000).

[g] Uncertainty reported is percent two-sigma standard error for individual analyses shown. For averages of replicate analyses, uncertainty is propagated two-sigma standard error. With tailing effects and mass bias corrections the overall reproducibility on standards is 1–2% for all techniques (Sims et al., 2008a). Based on the interlaboratory blind assessment of standard values from Richter et al. (2006), interlab agreement on standard values by MC–ICP-MS techniques is expected to be on the order of ±1–2% for uranium isotope ratios. Internal uncertainty for ($^{234}U/^{238}U$) by MC–ICP-MS techniques for low-level volcanic rocks is typically 0.5–0.6% (e.g. Rubin et al., 2005), when uncertainties in mass bias corrections, tailing corrections, and corrections between detectors are considered. Internal standard reproducibility results for all laboratories are as reported in Sims et al. (2008a).

[h] Pa concentration and isotopic standard analyses and uncertainties are as reported in Prytulak et al. (2008).

[i] Sample POS210/1 702 DS-1 has measured ($^{226}Ra/^{230}Th$) = 1.10 ± 3% (2σ standard error).

[j] ($^{234}U/^{238}U$) was measured to determine sample contamination by seawater. Data do not exist for the early TIMS data sets from Amsterdam and LANL, or for one unsuccessful sample analysis at WHOI (a replicate measurement of sample POLARK7-1-21847). Analyses with ($^{234}U/^{238}U$) in equilibrium are considered unaltered, as explained in the text, and are indicated in bold.

[k] $(^{231}Pa/^{235}U)_{max}$ indicates maximum ($^{231}Pa/^{235}U$) ratios corrected to hypothesized zero-age values if the samples are 10,000 years old, as described in the text.

[l] $(^{230}Th/^{238}U)_c$ indicates linearly corrected ($^{230}Th/^{238}U$) values to ($^{234}U/^{238}U$) = 1.000, indicating minimal seawater alteration, as described in the text.

et al. (2008)), and at the University of Bristol (methods as described in Regelous et al. (2004), Hoffmann et al. (2007), Prytulak et al. (2008), and Sims et al. (2008b)). Good agreement of U-series data from these two laboratories has been documented through U (Richter et al., 2006) and Th (Sims et al., 2008a) laboratory inter-calibration exercises. Several replicate samples in this current study (Table 2) serve as further comparisons using more challenging materials with lower Th and U abundances. Although the analytical details are comprehensively reported elsewhere, some salient points are summarized below.

This paper also includes a few older but previously unpublished thermal ionization mass spectrometry (TIMS) [U], [Th], and (^{230}Th/^{232}Th) data produced by: (1) K. Sims and M. Murrell at Los Alamos National Laboratory (LANL) using methods described in Sims et al. (1995, 1999) and Goldstein et al. (1989); and (2) T. Elliott and N. Mattelli at Faculteit der Aardenschappen, Vrije Universiteit (VU), Amsterdam using methods similar to those described in Frujiter et al. (2000), although samples were analyzed using single filaments loaded with graphite rather than double filaments. The good agreement demonstrates that the quality of TIMS data is generally comparable to that of ICP-MS data in this study (e.g. 2–3% 2σ uncertainties reported for isotope ratios measured by TIMS methods; see Table 2).

3.1.1. U–Th concentrations

Uranium and Th concentrations were analyzed by isotope dilution ICP-MS using a Thermo Element2 mass spectrometer at WHOI and by MC–ICP-MS using a ThermoFinnigan Neptune instrument at Bristol. Analyses at WHOI follow procedures outlined in Sims et al. (2008b): all measurements were conducted in pulse counting mode on the Element2 instrument, with additional analysis of intermediate mass steps to assess the effects of tailing on the 233 amu mass peak, and a separate scan to calculate a background correction. Mass bias is corrected using a linear interpolation of standard-sample-standard measurements of the ^{235}U/^{238}U mass ratio in standard NBL-112A, with all samples measured in triplicate. Calibrations of the ^{238}U and ^{232}Th standards (NBS960 and Ames, respectively) are known to a 2σ precision of 1%. Our results for standards analyzed as unknowns within sample batches (Table 2) are consistent with the inter-laboratory comparison of standard analyses evaluated in Sims et al. (2008a,b). Analyses conducted at the University of Bristol follow the procedure of Hoffmann et al. (2007), with similar uncertainties; we note that, unlike the analytical procedures used at WHOI, Bristol concentration measurements were conducted simultaneously with isotopic composition analyses (see further details below). A gravimetrically calibrated ^{229}Th–^{236}U double spike was used to determine concentrations.

Overall, U and Th concentration and corresponding (^{238}U/^{232}Th) isotope data measured in replicate in the different laboratories are in excellent agreement within reported 2σ uncertainties. The one exception is sample TRI0139-015-001G, for which the analytical results at WHOI and Bristol are not in agreement within 2σ uncertainties. Since the three measured (^{234}U/^{238}U) isotope ratios for this sample cover a range from within equilibrium (1.003) to out of equilibrium (1.007), we suspect sample heterogeneity and/or variable alteration/contamination. In particular, we note the WHOI analysis was conducted using ~5 g of hand-picked glass chips in an unsuccessful attempt to obtain a sufficient quantity of the sample for Ra isotopic analysis, while the previous Bristol analyses were conducted using only ~0.6 g of hand-picked sample material. We posit that this sample is variably contaminated. As explained below (see Section 4), electron microprobe analytical results for sample TRI0139-015-001G revealed a wide range of Cl/K_2O within a single glass chip, suggesting small-scale variations in glass composition.

3.1.2. ($^{234}U/^{238}U$) activity ratios

All (^{234}U/^{238}U) analyses were done by MC–ICP-MS. Kolbeinsey Ridge samples have extremely low concentrations of U (down to 0.01 μg/g), requiring large amounts of material to be picked and processed to obtain precisions below 0.5%.

Our analytical methods at the WHOI facility produced uncertainties in keeping with the findings of Richter et al. (2006), and as previously reported by Ball et al. (2008) and Sims et al. (2008b). During analysis of U isotopes using the facility's ThermoFinnigan Neptune, we calibrated SEM yield and simultaneously corrected for mass bias with standard-sample-standard bracketing to monitor SEM efficiency and measurement of the standard U010. Ball et al. (2008) observed that the SEM yield correction is error limiting for these analyses. Mass bias drift is corrected and SEM yield is calibrated using U010 corrections (Ball et al., 2008), and mass bias corrections are made using a linear interpolation of U010 ^{238}U/^{236}U = 14,535 ± 149 (Sims et al., 2008b). The sensitivity of U using this method is 0.1% ion yield (Sims et al., 2008b). The accuracy of U isotope analyses by this method is 0.5% for rock standards (Ball et al., 2008), with an internal reproducibility of 0.2–0.5% (2σ) (Sims et al., 2008b). All measured U isotope compositions reported in Table 2 were corrected after sample-standard bracketing with the U010 standard as calibrator, using a standard ^{234}U/^{238}U ratio of 5.4484×10^{-5} (Richter et al., 2006), and then corrected again using the U960 standard, which was analyzed several times during most analytical sessions and was assumed to have an accepted ^{234}U/^{238}U ratio of 5.286×10^{-5} (Richter et al., 2006).

Analytical procedures used by the Bristol Isotope Group are documented in some detail by Hoffmann et al. (2007), who also discuss the Bristol data in the light of the European Commission U isotope inter-calibration exercise (Richter et al., 2006). The behavior of the SEM was characterized as described in Hoffmann et al. (2005), but the multiplier currently in use is more linear (see Hoffmann et al., 2007) than that described in the earlier publication. Static measurements of ^{235}U/^{238}U and ^{234}U/^{238}U are made on standard material NBL-112a to give instrumental mass bias and SEM-faraday yields, using reference ratios of 0.007252618 and 5.54887×10^{-5}, respectively. Values of mass bias and yield for samples are calculated by linear interpolation of the measurements made on bracketing

NBL112a analyses. Samples are introduced using an Aridus desolvation device and a nominal 50 μl/min nebulizer, which yield ~100pA beams for a 30 ppb U solution. This approach yields ($^{234}U/^{238}U$) of unity with variability of less than 3 per mil for three commonly used secular equilibrium standards (Hoffmann et al., 2007). Here, we have monitored reproducibility of the standard BCR over the course of this study, which contains considerably more U than the samples but presents the advantage of a basaltic matrix. We obtained ($^{234}U/^{238}U$) = 1.003 ± 0.004 (2σ) for nine measurements on six separate dissolutions (Table 2). From this and other work it appears that this rock standard is not in secular equilibrium to better than ~1% (Hoffmann et al., 2007; Prytulak et al., 2008).

Overall agreement of replicates between the WHOI and Bristol facilities is within 2σ analytical uncertainties, with the exception of samples TRI0139-006-002G and TRI0139-015-001G. As explained above for TRI0139-015-001G, this variation may reflect a particularly heterogeneous sample composition.

Our reported 2σ standard deviation uncertainties of 0.5% are based on multiple digestions of rock standards and are consistent both with other studies (Rubin et al., 2005; Sims et al., 2008a; Koornneef et al., 2010) and with expectations of propagated errors based on the blind study of synthetic standards reported in Richter et al. (2006).

3.1.3. ($^{230}Th/^{232}Th$) activity ratios

Kolbeinsey Ridge samples have extremely low concentrations of Th, which, as for U, means that large amounts of sample (~0.5 g) have to be picked and processed in order to generate sufficiently precise analyses.

The MC–ICP-MS analytical protocols at WHOI followed those outlined by Hoffmann et al. (2007), Ball et al. (2008), and Sims et al. (2008a). The MC–ICP-MS methods at WHOI include an offline, exponential tailing correction of the 232 amu mass peak on the ^{230}Th peak, which has been found to be considerably more accurate than linear corrections for Th isotopes, which overestimate the tailing of mass ^{232}Th on ^{230}Th (Ball et al., 2008). For bracketing standard analyses, this correction is ratioed to a theoretical ratio, correcting for both mass bias and SEM efficiency (Ball et al., 2008). The tailing correction amounts to a smaller source of uncertainty than the mass bias correction, however, which is more difficult for Th than for U isotopic analyses: older methods of correcting for mass bias using U isotopes have been found to be problematic (Hoffmann et al., 2007; Ball et al., 2008; Sims et al., 2008a), producing systematically low $^{230}Th/^{232}Th$ ratio measurements (Sims et al., 2008a). Bracketing with a Th standard is, thus, essential. For this study we used the well-characterized standard UCSC Th 'A', which has a $^{230}Th/^{232}Th$ ratio of $5.856 \pm 0.070 \times 10^{-6}$ (Rubin, 2001), and applied a linear interpolation to correct the $^{230}Th/^{232}Th$ ratio (Sims et al., 2008a). The drift correction using this standard was found to be 0.5–1.0% (Sims et al., 2008b). Reported 2σ uncertainties for standard analyses at WHOI are 0.4–0.9% (Ball et al., 2008), and interlaboratory agreement for $^{230}Th/^{232}Th$ ratios in rock standards is as good as 1% (Sims et al., 2008a).

Methods for MC–ICP-MS analysis of Th isotopes at Bristol follow those reported (Hoffmann et al., 2007). For the Bristol analyses, samples are bracketed by an in-house standard, TEDDi, which has carefully calibrated $^{230}Th/^{232}Th$ and $^{229}Th/^{232}Th$ ratios (Hoffmann et al., 2007). These two ratios are used for yield and mass bias calculations, which are linearly interpolated between standard runs for data reduction of samples. TEDDi was designed for carbonate sample measurement and a long washout is required to reduce the typically more intense ^{232}Th beams (~100 pA) used in silicate analyses to levels that do not influence the measurement of the ~2pA ^{232}Th intensity of the standard. A tailing correction on masses 230 and 229 is calculated for each sample by interpolating an exponential curve, which is obtained by a best fit routine applied to intensities measured at 228.5, 229.5, 230.5, 231 and 231.5 amu. ^{238}U–^{230}Th disequilibrium measurements for the standards TML and BCR2 measured over the course of this study are reported in Table 2. They agree within error of the WHOI analyses and data reported in Hoffmann et al. (2007), Prytulak et al. (2008), and Sims et al. (2008a).

Again, the $^{230}Th/^{232}Th$ isotopic ratios are in excellent agreement between laboratories, with the exception of one sample, TRI0139-015-001G. As discussed above, because this sample is altered we surmise that the discrepant analyses reflect heterogeneity in sample alteration signatures.

3.1.4. ^{226}Ra concentrations

Radium concentration in sample POS210/1 702DS-1 was measured at WHOI by MC–ICP-MS using methods described in Sims et al. (2008b) (Table 2 footnote). We used a ^{228}Ra spike that has been calibrated against the NIST4967 ^{226}Ra standard (characterized within 1.18% 2σ uncertainty). Background corrections were made with a peak-hopping routine on the SEM detector, and mass bias corrections were conducted using U isotopes measured in the standard NBL-112A. Rock standards TML and AThO have been reliably measured in equilibrium within 1% uncertainty (2σ). Other laboratories report uncertainties based on internal precisions and short-term reproducibility of single dissolutions (e.g. Pietruszka et al., 2011), but we note that the uncertainty in these analyses is limited by our knowledge of the NIST4967 ^{226}Ra standard (1.2%) used for spike calibration, so we take a robust approach by incorporating this uncertainty into our error calculations. Our uncertainties in these measurements are comparable to those reported from other laboratories (e.g. Koornneef et al., 2010).

3.1.5. ^{231}Pa concentrations

Protactinium isotopic concentrations were measured by a MC–ICP-MS Neptune at Bristol using the methods presented in Regelous et al. (2004) and Prytulak et al. (2008). The standard NBL-112a is added to the separated Pa, such that simultaneous measurement of ^{238}U and ^{235}U on Faraday cups with ^{233}Pa on the SEM allows for correction for beam instability and mass bias. Monitoring the ^{232}Th peak enables us to assess hydride interferences on ^{233}Pa isotopes, but this effect has been found to be insignificant in properly separated samples (Regelous et al., 2004). Reported internal

Table 3
Measured radiogenic isotope data for samples lacking previous literature analyses, including new cruise samples (POS 326).

Sample	Location	$^{143}Nd/^{144}Nd$[a]	±[d]	ε_{Nd}	$^{176}Hf/^{177}Hf$[a]	±	ε_{Hf}	$^{87}Sr/^{86}Sr$[c]	±	$^{206}Pb/^{204}Pb$[c]	±	$^{207}Pb/^{204}Pb$[c]	±	$^{208}Pb/^{204}Pb$[c]	±
POS185 1105B	Tjörnes FZ	0.513108	0.000007	9.2	0.283282	0.000006	18.0								
POS185 1093	S. Kolbeinsey	0.513096	0.000005	8.9	0.283281	0.000004	18.0								
POS291 485-3	S. Kolbeinsey	0.513121	0.000009	9.4	0.283208	0.000036	15.4								
POS326 540DS-4	S. Kolbeinsey	0.513142	0.000008	9.8	0.283270	0.000016	17.6								
POS291 495-2	S. Kolbeinsey	0.513136	0.000013	9.7	0.283280	0.000014	18.0	0.702893	0.000010	18.0423	0.0003	15.4338	0.0003	37.7547	0.0006
POS185 1096A	S. Kolbeinsey	0.513143	0.000050	9.9	0.283280	0.000003	18.0	0.702880	0.000010						
POS185 1096A(rep)	S. Kolbeinsey	0.513143[b]	0.000008	9.9											
POS185 1094B	S. Kolbeinsey	0.513096[b]	0.000006	8.9	0.283280	0.000005	18.0	0.702938	0.000010	18.062	0.002	15.441	0.002	37.805	0.005
POS0002/2 Geo 212	S. Kolbeinsey	0.513133	0.000005	9.7	0.283287	0.000005	18.2	0.702737	0.000010						
POS221 596DS-1	S. Kolbeinsey	0.513162	0.000006	10.2	0.283303	0.000007	18.8	0.702737	0.000010						
POS221 605DS-2	S. Kolbeinsey	0.513160	0.000007	10.2	0.283305	0.000010	18.9	0.702701	0.000010	17.9394	0.0003	15.4150	0.0003	37.5584	0.0009
POS221 605DS-2(rep)	S. Kolbeinsey	0.513153[b]	0.000012	10.1											
POS210/1 682DS-1	N. Kolbeinsey	0.513159[b]	0.000009	10.2	0.283314	0.000005	19.2	0.702714	0.000010						
POLARK7-1-21844	N. Kolbeinsey	0.513136	0.000009	9.7	0.283302	0.000006	18.7								
POLARK7-1-21847	N. Kolbeinsey	0.513102	0.000005	9.1	0.283261	0.000005	17.3								
POLARK7-1-21848	N. Kolbeinsey	0.513142	0.000005	9.8	0.283297	0.000005	18.6								
POLARK7-1-21850	N. Kolbeinsey	0.513176	0.000010	10.5	0.283316	0.000020	19.2								
POLARK7-1-21854	N. Kolbeinsey	0.513146	0.000005	9.9	0.283293	0.000004	18.4								
POLARK7-1-21856-3	N. Kolbeinsey	0.513139	0.000005	9.8	0.283279	0.000007	17.9								
POS210/1 702 DS-1	Eggvin Bank	0.513053	0.000007	8.1	0.283225	0.000012	16.0								
POS210/1 700 DS-2	Eggvin Bank	0.513014	0.000004	7.3	0.283195	0.000009	15.0								
POS210/1 698 DS-1	Eggvin Bank				0.283205	0.000008	15.3								

[a] $^{176}Hf/^{177}Hf$ and $^{143}Nd/^{144}Nd$ measured by MC–ICP-MS at Ecole Normale Supérieure de Lyon, and are normalized relative to $^{179}Hf/^{177}Hf = 0.7325$ and $^{146}Nd/^{144}Nd = 0.7219$, respectively. $^{176}Hf/^{177}Hf$ of JMC-475 Hf standard = 0.282160 ± 0.000010 ($n = 15$); $^{143}Nd/^{144}Nd$ of Rennes in-house standard = 0.511961 ± 0.000013 ($n = 50$) (Chauvel and Blichert-Toft, 2001).

[b] $^{143}Nd/^{144}Nd$ for samples POS185 1096A(rep), POS221 605DS-2(rep), POS185 1904B, and POS210/1 682DS-1 measured by MC–ICP-MS (ThermoFinnigan Neptune) at WHOI and are normalized relative to 0.7219. $^{143}Nd/^{144}Nd$ of La Jolla Nd standard = 0.511847 ± 0.000015.

[c] $^{87}Sr/^{86}Sr$, $^{206}Pb/^{204}Pb$, $^{207}Pb/^{204}Pb$, and $^{208}Pb/^{204}Pb$ measured by MC–ICP-MS (ThermoFinnigan Neptune) at WHOI. Sr data are corrected using standard NBS987 $^{87}Sr/^{86}Sr = 0.710240 \pm 0.000026$. and Pb data using standard NBS981 $^{206}Pb/^{204}Pb = 16.9356$, $^{207}Pb/^{204}Pb = 15.4891$, and $^{208}Pb/^{204}Pb = 36.7006$; internal precisions for these ratios ranges from 15 to 30 ppm, and external reproducibility ranges from 17 ppm for $^{207}Pb/^{204}Pb$ to 117 ppm for $^{208}Pb/^{204}Pb$ (Hart and Blusztajn, 2006). Samples to be analyzed for Pb were compared with an internal Tl standard, and by repeat analysis of NBS981 (Hart and Blusztajn, 2006; Sims and Hart, 2006). Sample POS185 1094B has higher uncertainties than other samples due to its overall lower trace element abundances.

[d] Uncertainties are 2σ standard errors for all isotopic analyses.

precisions using these methods are 0.5% (2σ). External reproducibility of (^{231}Pa/^{235}U) assessed from 10 independent dissolutions and measurements of BCR is ±1.3% (2σ), as reported by Prytulak et al. (2008). Some of the BCR measurements reported by Prytulak et al. (2008) were made over the course of this study and the average of this sub-set is reported in Table 2. Count rates for Kolbeinsey Ridge samples ranged from 80–1400 cps and 400–900 cps for masses 231 and 233 amu, respectively, and corresponding ^{231}Pa/^{233}Pa ratios ranged from 0.1 to 0.9 for the sample suite. As reported in Table 2, uncertainties for these runs were relatively low despite the low Pa and U abundances present in Kolbeinsey Ridge MORB; we attribute these results to our practice of processing greater than 0.6 g of separated glass chips per sample for ^{235}U–^{231}Pa analysis.

3.2. Nd–Sr–Hf–Pb isotopes

Neodymium and Hf isotope compositions were measured by MC–ICP-MS at either the Ecole Normale Supérieure (ENS) in Lyon (methods as in Blichert-Toft (2001) and Blichert-Toft et al. (2005, 1997)), where sample preparation included a stronger leaching step (20 min in 10% hydrochloric acid) or at WHOI (using the weaker leaching procedure described above in Section 3.1). Strontium and Pb isotopes were analyzed by MC–ICP-MS at WHOI (Hart and Blusztajn, 2006; Sims and Hart, 2006).

As reported in Hart and Blusztajn (2006), methods employed at WHOI for Nd isotope measurements result in measured precisions for individual runs ranging from 5 to 10 ppm (2σ). Sample ratios are adjusted to the LaJolla Nd standard assuming a standard ^{143}Nd/^{144}Nd ratio of 0.511847. Measured external precisions range from 15 to 25 ppm (2σ). Nd isotope measurements at the ENS facility were done using MC–ICP-MS methods after Blichert-Toft (2001). All resulting isotopic ratios were normalized relative to 0.7219, and adjusted to an in-house standard ("Rennes") with ^{143}Nd/^{144}Nd of 0.511961 ± 0.000013 (Chauvel and Blichert-Toft, 2001). Typical internal precisions range from 4 to 10 ppm (2σ). Two samples (POS185 1096A and POS221 605DS-2) replicated at both facilities have measured ^{143}Nd/^{144}Nd ratios in excellent agreement within uncertainty (Table 3).

Strontium isotopes were analyzed using a ThermoFinnigan Neptune MC–ICP-MS at WHOI, based on methods presented in Hart and Blusztajn (2006) and Jackson and Hart (2006). Precision and accuracy resembles Nd isotope uncertainties, with ^{87}Sr/^{86}Sr sample ratios adjusted using the standard SRM987 ratio of 0.7102140.

Hafnium isotopes were measured by MC–ICP-MS at ENS using methods after Blichert-Toft et al. (1997) and Blichert-Toft (2001). Sample ratios are normalized using a ^{179}Hf/^{177}Hf ratio of 0.7325, and all are adjusted with the JMC-475 Hf standard assuming a standard ^{176}Hf/^{177}Hf ratio of 0.28216 ± 0.00001. Reported rock standard uncertainties from Blichert-Toft (2001) for this method range from 0.0014% to 0.005% (2σ).

Lead isotopes were measured by MC–ICP-MS at WHOI and have internal precisions for ^{206}Pb/^{204}Pb, ^{207}Pb/^{204}Pb, and ^{206}Pb/^{204}Pb ratios ranging from 15 to 30 ppm (Hart and Blusztajn, 2006). External reproducibility ranges from 17 ppm (for ^{207}Pb/^{204}Pb) to 117 ppm (for ^{208}Pb/^{204}Pb). All ratios are corrected to standard SRM981 using values from Todt et al. (1996), with reproducibilities of less than 10 ppm for ^{206}Pb/^{204}Pb, ^{207}Pb/^{204}Pb, and ^{208}Pb/^{204}Pb ratios and less than 1.5 ppm for ^{206}Pb/^{208}Pb ratios.

3.3. Electron microprobe analysis

Major element and Cl and F concentrations were measured on hand-picked, unleached glass chips with a Cameca

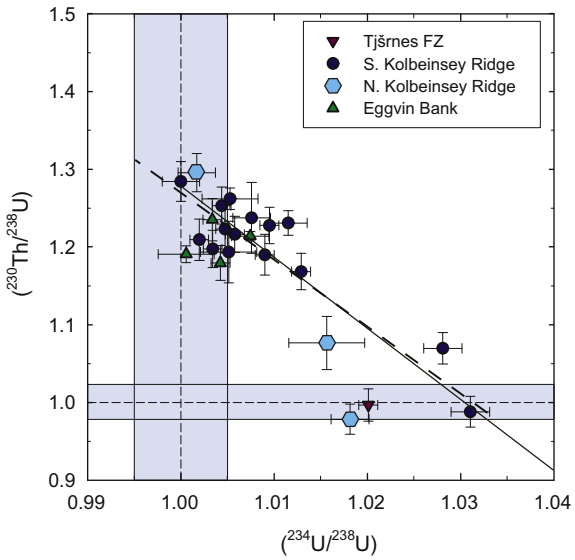

Fig. 2. (^{234}U/^{238}U) vs. (^{230}Th/^{238}U) for Kolbeinsey Ridge samples. Shaded regions are in equilibrium within analytical capabilities. The solid line shows a calculated theoretical trajectory for the addition of seawater to the average, unaltered Kolbeinsey Ridge sample composition. This binary mixing curve is calculated for an average of Kolbeinsey Ridge samples with (^{234}U/^{238}U) in equilibrium and seawater. Seawater (^{234}U/^{238}U) = 1.14 and (^{230}Th/^{238}U) = 1.1 × 10^{-4}, using ^{230}Th concentrations of 0.26 dpm/1000 L (2.5 × 10^{-17} mol/L), based on the nearest dissolved ^{230}Th measurement to the ridge reported in the compilation by Moran et al. (2001), and average ocean [U] = 3.3 ppb (1.4 × 10^{-8} mol/L). These low ^{230}Th values reflect the relatively high productivity in the Arctic Ocean (e.g. Zou, 1998). While U concentration is salinity-dependent, and can be affected by local groundwater and hydrothermal inputs (e.g. Charette et al., 2008), for these calculations we treat the oceans as well-mixed with respect to U (Ku et al., 1977). A non-linear best fit mixing curve using the method of Sohn (2005) for the Kolbeinsey data set, excluding samples north of 70.7°N on the ridge, is shown using a dashed line for comparison. This fitting method results in a trajectory with mixing end members at (^{234}U/^{238}U) = 0.995 ± 0.0007 and (^{230}Th/^{238}U) = 1.313 ± 0.01 and (^{234}U/^{238}U) = 1.033 ± 0.001 and (^{230}Th/^{238}U) = 0.983 ± 0.02, but we consider these values poorly resolved because of data scatter and the near-linearity of the fit (the best-fit method finds a hyperbolic mixing ratio of 1.009, which is within uncertainty of a linear relationship). Including Eggvin Bank samples results in slightly different results of (^{234}U/^{238}U) = 0.995 ± 0.0008 and (^{230}Th/^{238}U) = 1.317 ± 0.01 and (^{234}U/^{238}U) = 1.033 ± 0.001 and (^{230}Th/^{238}U) = 0.985 ± 0.02, with a hyperbolic mixing ratio of 1.026, i.e. also nearly linear.

SX-100 electron microprobe located at New Mexico Institute of Mining and Technology using standard electron microprobe techniques (Supplementary Table 1). Samples were first examined using backscattered-electron (BSE) imagery to confirm the presence of basaltic glass, and selected areas of glass were then quantitatively analyzed. Concentrations presented in Supplementary Table 1 are averages of multiple *in situ* measurements.

4. RESULTS

Table 1 lists Kolbeinsey Ridge sample locations, descriptions, and research cruises for the material used in this study. Uranium-series analyses are reported in Table 2, and Sr, Nd, Hf, and Pb isotope results are presented in Table 3 (see Supplementary Tables for the results of major element analyses of 26 samples and trace element analyses of five samples). Kolbeinsey Ridge samples are tholeiites characterized by extreme depletion in incompatible elements, with samples TRI0139-001-001G and POS185 1105B having, respectively, the lowest U and Th concentrations thus far measured in any MORB (Table 2). Results of electron probe major element analyses (Supplementary Table 1) are within uncertainty of published results for those samples already analyzed in the literature (Sigurdsson, 1981; Schilling et al., 1983; Mertz and Haase, 1997).

The activity ratio ($^{234}U/^{238}U$) is a sensitive indicator of secondary alteration processes since seawater is significantly enriched in ^{234}U relative to ^{238}U ($(^{234}U/^{238}U)_{sw} = 1.14$) (Thurber, 1962; Turekian and Bertine, 1971; Ku et al., 1977; Macdougall et al., 1979; Henderson et al., 1993; Cheng et al., 2000; Robinson et al., 2004). Twelve samples have ($^{234}U/^{238}U$) activity ratios greater than 1.000 ± 0.005 and are thus considered contaminated by interaction with seawater, given our analytical uncertainties (Fig. 2 and Table 2; see Section 5.1 for further discussion of these data).

Consistent with previous studies (Schilling et al., 1999; Tronnes et al., 1999; Haase et al., 2003; Mertz et al., 2004; Blichert-Toft et al., 2005), radiogenic isotopic compo-

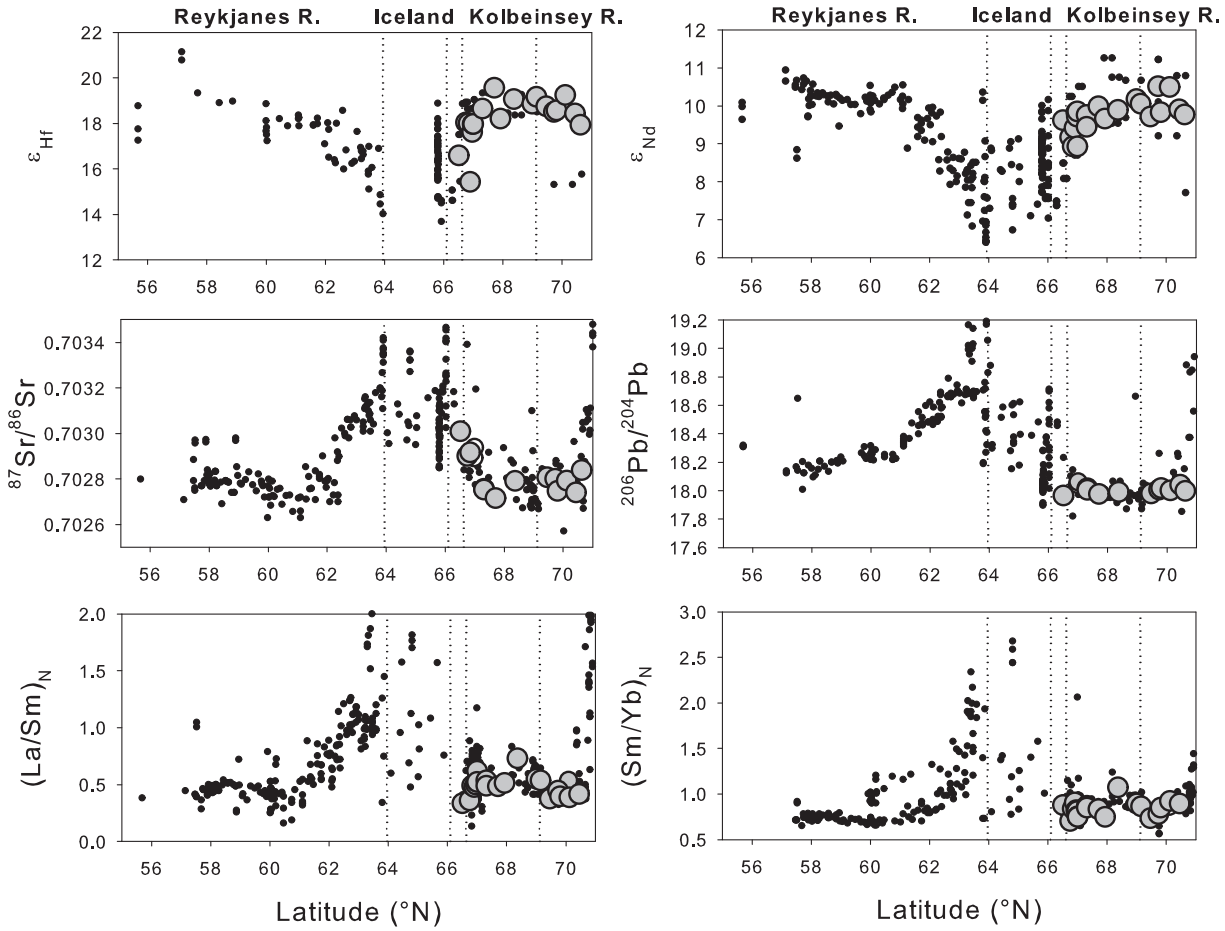

Fig. 3. Along-axis variations in trace element ratios and long-lived radiogenic isotopic ratios for the Reykjanes Ridge, Iceland, and the Kolbeinsey Ridge. Literature data shown as small black data points (O'Nions and Pankhurst, 1973; Schilling, 1975; Sun and Jahn, 1975; Cohen et al., 1980; Dupre and Allegre, 1980; Condomines et al., 1981; Schilling et al., 1983, 1999; Neumann and Schilling, 1984; Poreda et al., 1986; Furman et al., 1991; Mertz et al., 1991; Hemond et al., 1993; Devey et al., 1994; Hards et al., 1995; Hardarson and Fitton, 1997; Mertz and Haase, 1997; Salters and White, 1998; Stecher et al., 1999; Hanan et al., 2000; Hilton et al., 2000; Peate et al., 2001; Murton et al., 2002; Haase et al., 2003; Stracke et al., 2003a,b, 2006; Thirlwall et al., 2004; Blichert-Toft et al., 2005). Data for samples measured in this study are shown as gray circles.

sitions for Kolbeinsey samples south of 70.7°N are depleted (e.g. $\varepsilon_{Nd} = +8.4$ to $+10.5$, $\varepsilon_{Hf} = +15.4$ to $+19.2$, $^{87}Sr/^{86}Sr = 0.70272–0.70301$), while the three unaltered samples north of 70.7°N have relatively enriched isotopic signatures ($\varepsilon_{Nd} = +7.3$ to $+8.1$, $\varepsilon_{Hf} = +15.0$ to $+16.0$, $^{87}Sr/^{86}Sr = 0.70306–0.70309$). These samples, which are closer to the Jan Mayen Fracture Zone, also have lower ($^{238}U/^{232}Th$) ratios than samples along the rest of the Kolbeinsey Ridge (Figs. 3 and 4).

In Fig. 4 we show results for ($^{238}U/^{232}Th$) vs. ($^{230}Th/^{232}Th$) in our data set, distinguished by ($^{234}U/^{238}U$) filtering criteria (described in more detail above and in Section 5.1). Excluding the lower-($^{238}U/^{232}Th$) samples collected from the Eggvin Bank, the remaining data form a nearly horizontal array (slope = 0.6 ± 0.04), with relatively constant ($^{230}Th/^{232}Th$) (1.20–1.32) over a larger range in ($^{238}U/^{232}Th$) (0.94–1.32). However, this array is essentially defined by the samples at high ($^{238}U/^{232}Th$) for which ^{238}U–^{234}U is out of equilibrium or for which we have no ($^{234}U/^{238}U$) measurements.

The four unaltered and uncontaminated Kolbeinsey samples with ^{235}U-^{231}Pa measurements have ^{231}Pa excesses similar to those typically seen in MORB (($^{231}Pa/^{235}U$) ranging from 1.22 to 2.50, averaging 2.12; Fig. 5) (Goldstein et al., 1993; Pickett and Murrell, 1997; Lundstrom et al., 1998b; Sims et al., 2002, 2008b; Lundstrom, 2003; Bourdon et al., 2005). Sample POS210/1 700DS-2, which was collected at latitude 70.85°N on the Eggvin Bank and has relatively enriched radiogenic isotope signatures (e.g. $^{87}Sr/^{86}Sr = 0.70306$) (Haase et al., 2003) and trace element ratios ($U/Th = 0.26$; $La/Sm_N = 1.95$), has the lowest ($^{231}Pa/^{235}U$) = 1.22. The other three samples were collected further south on the Kolbeinsey Ridge and are more depleted ($\varepsilon_{Nd} = +8.9$ to $+10.0$ (Schilling et al., 1999),

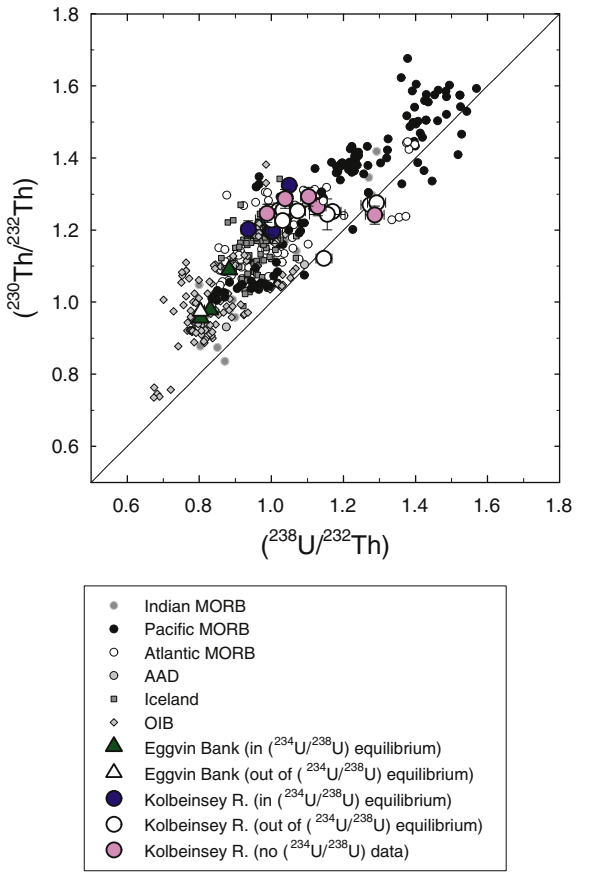

Fig. 4. ($^{230}Th/^{232}Th$) versus ($^{238}U/^{232}Th$) "equiline" diagram for Kolbeinsey basalts. Data are broken out by determination of crustal contamination from measurements of ($^{234}U/^{238}U$). For comparison we show global Atlantic, Pacific, Indian, and Australian–Antarctic (AAD) MORB data (Goldstein et al., 1989, 1992, 1993; Sims et al., 1995, 2002; Bourdon et al., 1996b; Lundstrom et al., 1999; Sturm et al., 2000; Peate et al., 2001; Tepley et al., 2004; Kokfelt et al., 2005; Russo et al., 2009; Standish and Sims, 2010), global ocean island basalt (OIB) data (except for Iceland) (Sims et al., 1995, 1999, 2008b; Turner et al., 1997; Widom et al., 1997; Bourdon et al., 1998; Claude-Ivanaj et al., 1998; Sigmarsson et al., 1998; Claude-Ivanaj et al., 2001; Pietruszka et al., 2001, 2009; Sims and Hart, 2006; Prytulak and Elliott, 2009), and Icelandic data (Kokfelt et al., 2003; Stracke et al., 2003a,b).

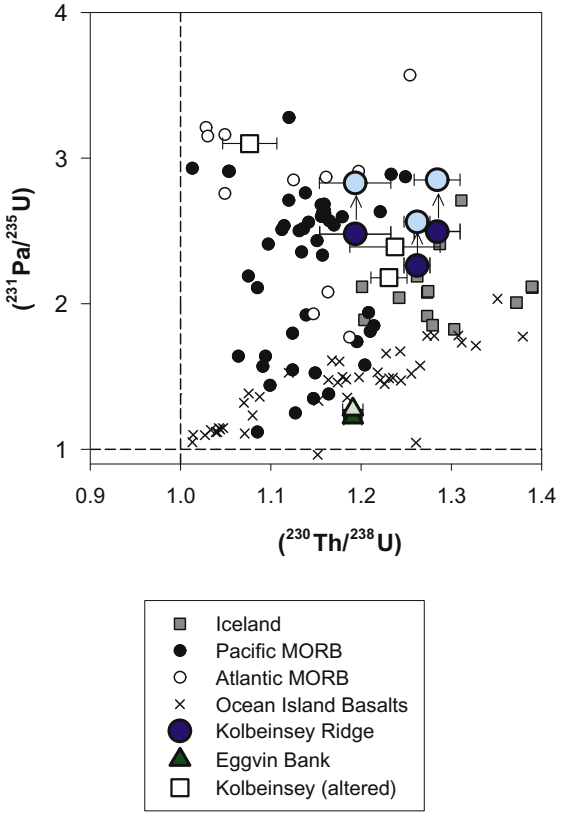

Fig. 5. ($^{230}Th/^{238}U$) vs. ($^{231}Pa/^{235}U$) data from the Kolbeinsey Ridge, Iceland (Pickett and Murrell, 1997; Stracke et al., 2006), global OIB (Sims et al., 1995, 1999, 2008b; Pickett and Murrell, 1997; Turner et al., 1997; Bourdon et al., 1998; Pietruszka et al., 2001; Sims and Hart, 2006; Prytulak and Elliott, 2009), and global MORB (Goldstein et al., 1993; Sims et al., 1995, 2002; Lundstrom et al., 1999; Sturm et al., 2000; Kokfelt et al., 2005). Here the lighter shaded circle and triangle data points show age-corrected maximum ($^{231}Pa/^{235}U$) values for Kolbeinsey Ridge south of the 70.7°N offset and from the Eggvin Bank, respectively (Table 2). We show Kolbeinsey Ridge samples known to be contaminated (($^{234}U/^{238}U$) out of equilibrium) for completeness.

U/Th = 0.31 to 0.35), with (^{231}Pa/^{235}U) = 2.26 to 2.50. There is no co-variation of (^{231}Pa/^{235}U) with other chemical parameters or geographic location (e.g. proximity to Iceland). Given the independent age constraint of $\leqslant$10,000 years for Kolbeinsey Ridge lavas (see Section 2.2), it is possible that the (^{231}Pa/^{235}U) ratios in the samples have decreased slightly due to aging since eruption. We have calculated the maximum possible (^{231}Pa/^{235}U) upon eruption for our samples by assuming they are 10,000 years old, and present those maximum values in Table 2 and depict them in Fig. 5 using lightly shaded symbols.

In Fig. 6 we show the results of Cl and K analyses by electron microprobe with the (^{234}U/^{238}U) results for our samples. We find no systematic correlation between these variables in the Kolbeinsey Ridge data set. We do, however, note that sample TRI0139-015-001G demonstrated a high degree of intra-sample variability, producing Cl/K_2O ratios ranging from 0.05 to 0.55 within a single glass chip.

5. GENESIS OF U-SERIES DISEQUILIBRIA IN KOLBEINSEY RIDGE BASALTS

5.1. Age constraints from U-series

Interpretation of ^{238}U–^{230}Th and ^{235}U–^{231}Pa disequilibria in terms of melting processes requires the age of the samples to be much younger than the half-lives of ^{230}Th (75 ka) and ^{231}Pa (32.5 ka). Recovery of fresh basaltic glass (rather than glacial outwash) constrains the ages of our samples to <10 ka, which results in a maximum uncertainty on the (^{230}Th/^{238}U) ratios due to post-eruptive decay of ~1%. Additionally, dredge sample POS210/1 702DS-1 has measured (^{226}Ra/^{230}Th) = 1.10 ± 3% (Table 2 footnote), since ^{226}Ra has a half-life of 1600 years, the small but significant ^{226}Ra/^{230}Th disequilibrium of this sample indicates that its age is younger than 8 ka. The influence of a maximum of 10,000 years of aging on Pa disequilibria results

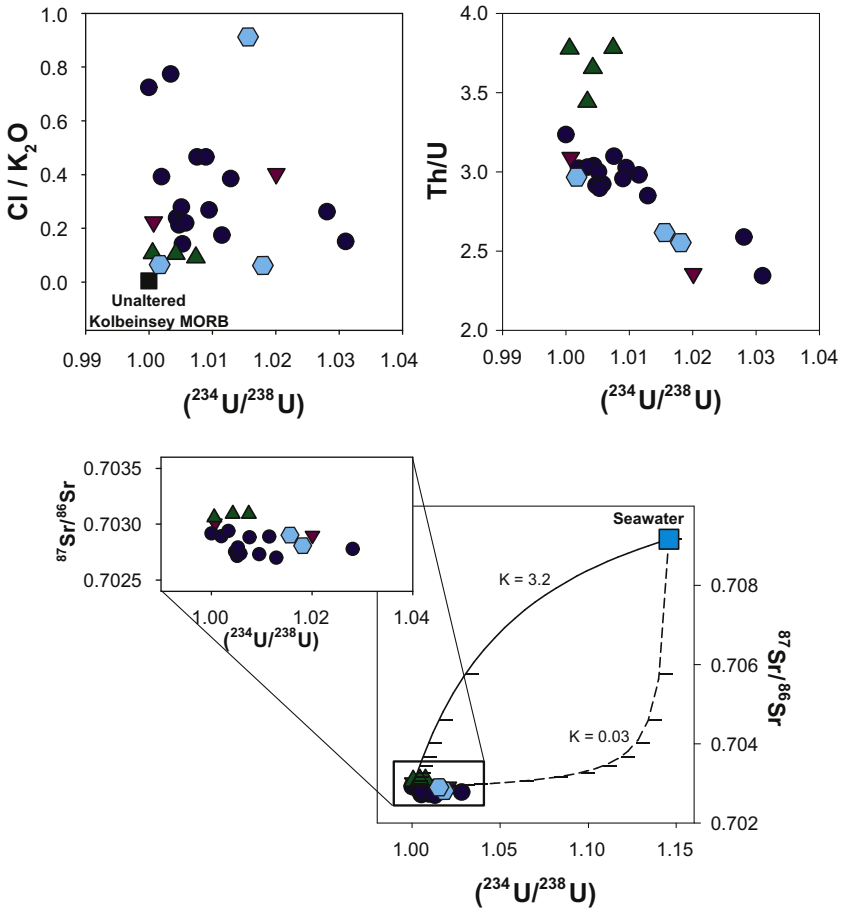

Fig. 6. (a) Measured Cl/K_2O vs. (^{234}U/^{238}U) for the Kolbeinsey Ridge. The lack of a systematic variation suggests that multiple decoupled contaminating or altering processes affect Cl abundances and U isotopes in basalts. Composition for unaffected N–MORB comes from suggested Cl/K N–MORB ratio from Michael and Cornell (1998). (b) (^{234}U/^{238}U) vs. Th/U ratios for data from this study, showing negative correlation for Kolbeinsey Ridge basalts. (c) Diagram of (^{234}U/^{238}U) vs. ^{87}Sr/^{86}Sr with Kolbeinsey Ridge data (inset shows expanded scale), with the two mixing trajectories described in the text shown as solid and dashed black lines. Tick marks show percentage mixtures of mixing components for each calculation, and labels show the K ratios that correspond to each hyperbolic binary mixing curve, where $K = (^{86}Sr_{sw} \times (^{238}U)_{KR\ MORB})/(^{86}Sr_{KR\ MORB} \times (^{238}U)_{sw})$ (as in e.g. Faure and Mensing (2005)) and "*sw*" indicates seawater and "*KR MORB*" indicates average, unaltered ((^{234}U/^{238}U) in equilibrium; Table 2) Kolbeinsey Ridge MORB. All symbols as in Fig. 2.

in differences of 4–14% in reported ($^{231}Pa/^{235}U$) ratios, and maximum age-corrected ($^{231}Pa/^{235}U$) values for samples erupted no more than 10,000 years ago are included in Table 2.

5.2. Effects of shallow alteration on ^{238}U–^{230}Th disequilibrium

Twelve samples have ($^{234}U/^{238}U$) > 1.005, despite careful hand-picking and leaching (see details above). These high ($^{234}U/^{238}U$) values are significantly outside of analytical uncertainty, and are thus interpreted to be a result of seawater interaction or assimilation of altered material (Fig. 2 and Table 2). Our criterion for considering our remaining samples unaltered and uncontaminated is when their uranium isotope ratios are within 0.5% of equilibrium (which reflects the propagated uncertainties of current analytical methods; see details above). Of the published MORB ICP-MS U-series literature data (Goldstein et al., 1989, 1992; Lundstrom et al., 1995, 1998a, 1999; Sims et al., 1995, 2002, 2003; Bourdon et al., 1996b; Sturm et al., 2000; Tepley et al., 2004; Kokfelt et al., 2005; Rubin

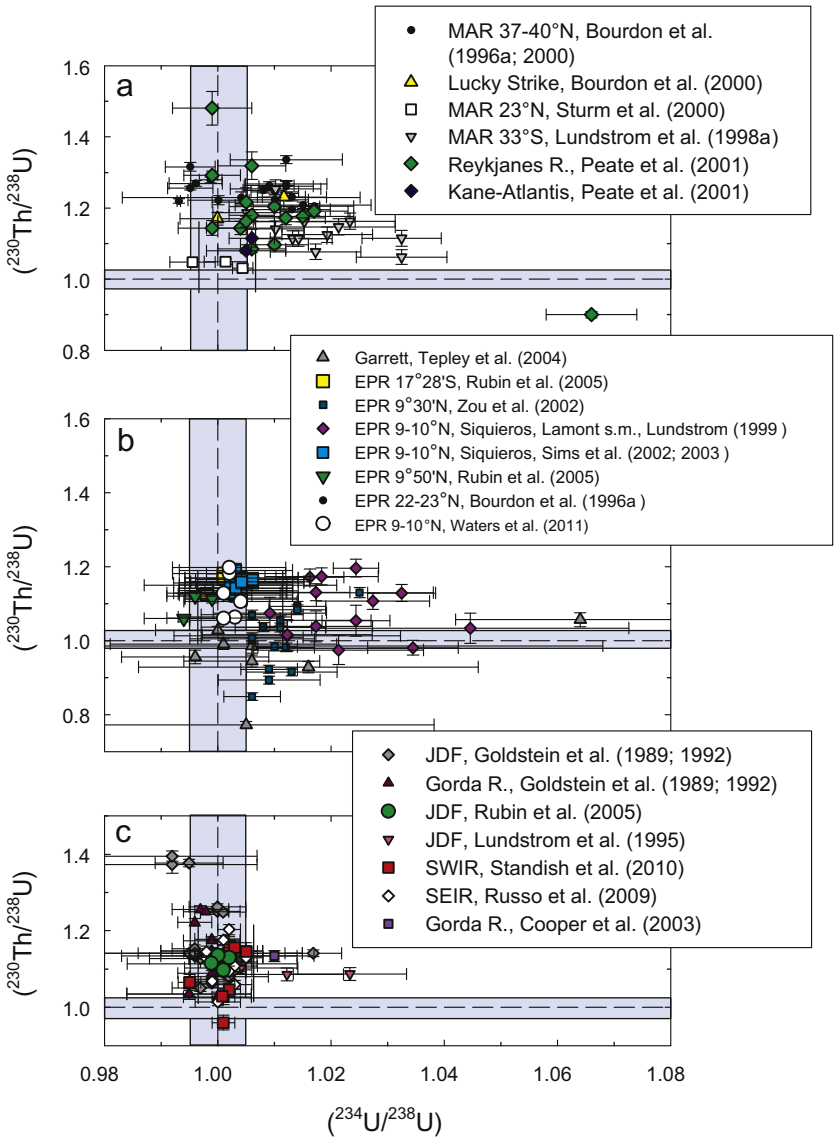

Fig. 7. Global ($^{234}U/^{238}U$) vs. ($^{230}Th/^{238}U$) MORB data from the literature with 2σ analytical uncertainties. (a) Mid-Atlantic Ridge (MAR) (b) East Pacific Rise (EPR), and (c) Juan de Fuca Ridge (JDF) and Indian Ocean data are shown as separate panels. We note that the large error bars reflect unusually large analytical uncertainties in data from Tepley et al. (2004). To address the problem of older studies using different values for isotope decay constants, we have corrected older literature to the newer decay constant value of Cheng et al. (2000). After doing so, we find very little or no systematic patterns to the global data set; however, since many of these data were measured by different mass spectrometric analytical techniques and may have incorporated inter-laboratory and other sample biases, it is unclear to what extent disequilibrium in the literature ($^{234}U/^{238}U$) ratios reflects natural alteration of fresh basalt samples rather than analytical problems. Unfortunately, we thus cannot be certain whether the samples from the literature with ($^{234}U/^{238}U$) out of equilibrium have experienced crustal alteration, or instead appear out of equilibrium due to older, less robust analytical methods. (See above-mentioned reference for further information.)

et al., 2005; Russo et al., 2009; Standish and Sims, 2010; Waters et al., 2011) only a limited selection of MORB measurements fit within a similar constraint (Fig. 7) (i.e. 9–10°N EPR (Sims et al., 2002, 2003; Rubin et al., 2005; Waters et al., 2011), Southwest Indian Ridge (Standish and Sims, 2010), Gorda Ridge (Goldstein et al., 1989, 1992; Cooper et al., 2003), 22–23°N EPR (Bourdon et al., 1996b), Mid-Atlantic Ridge (Sturm et al., 2000), and Kane-Atlantis (Peate et al., 2001)). Analyses conducted using older analytical methods with larger ($^{234}U/^{238}U$) uncertainties may also indicate relatively fresh samples unaffected by crustal processes, but this is more difficult to constrain due to the range of techniques and uncertainties in the older literature. Likewise, many older studies did not measure ($^{234}U/^{238}U$), such that this list also necessarily excludes more poorly characterized samples that may not have been contaminated or altered.

The Kolbeinsey Ridge ($^{234}U/^{238}U$) and ($^{230}Th/^{238}U$) vary systematically (Fig. 2): samples with low ($^{230}Th/^{238}U$) have high ($^{234}U/^{238}U$), whereas samples with high ($^{230}Th/^{238}U$) have equilibrium ($^{234}U/^{238}U$). Although a single, specific mechanism for the crustal perturbation of the ^{238}U-^{234}U–^{230}Th system has not been identified (see further discussion below), such signals are widely observed in submarine glass (e.g. Turekian and Bertine, 1971; Bacon, 1978; Macdougall et al., 1979; Sims et al., 2002, 2003, 2006; Pelt et al., 2008; Pietruszka et al., 2009, 2011), and therefore we interpret this relationship in terms of secondary processes, namely interaction with seawater-derived materials in the shallow crust. We note that for one sample (PO-LARK7-1-21854) with a ^{238}U excess (measured at LANL in the early 1990s) ($^{234}U/^{238}U$) was not measured, but given the observed relationship between ($^{234}U/^{238}U$) and ($^{230}Th/^{238}U$) it is likely that this sample has also experienced chemical exchange with crustal contaminants and we predict $(^{234}U/^{238}U) > 1$. Unfortunately this sample is no longer available to evaluate this, and to eliminate any inferential ambiguities in our subsequent interpretations this sample is not considered further. We further note that because the highly variable initial uranium concentrations in Kolbeinsey MORB (Table 2) could mask uranium addition processes, here we focus on the observed variations in elemental and isotopic ratios rather than elemental abundances.

Elevated uranium concentrations and ($^{234}U/^{238}U$) ratios have long been observed in basalts either contaminated in the crust or directly altered by seawater (Aumento, 1971; Turekian and Bertine, 1971; Störzer and Selo, 1976, 1978; Macdougall, 1977; Bacon, 1978; Macdougall et al., 1979; Bourdon et al., 2000; Sims et al., 2003, 2006). Turekian and Bertine (1971) suggested that addition of seawater-derived uranium to basalts occurred in the shallow crust or at the crust-water interface. Sims et al. (2003) likewise observed other chemical indications of contamination in a sample with $(^{234}U/^{238}U) = 1.009$, including perturbed Th/U, elevated Cl/K, high Ba/Th, a negative Ce anomaly, and elevated $^{87}Sr/^{86}Sr$.

A number of mechanisms may lead to chemical contamination of basaltic magmas in the crust. Magmas might interact with hydrothermal brines as they travel to the surface, as suggested by Michael and Cornell (1998), who found that at slow-spreading ridges with thick crust (namely the Kolbeinsey Ridge), magmas can pool relatively shallow in the crust and experience more crustal contamination than occurs on slow-spreading ridges with thinner crust (i.e. regions with lower magma flux). They measured high and variable Cl/K that was weakly correlated with MgO in Kolbeinsey MORB, which they interpreted to represent assimilation of hydrothermal brines, secondary minerals, and/or hydrothermally altered basalt during crystal fractionation in a magma chamber.

High Cl concentrations in crustally contaminated basalts have also been measured elsewhere (e.g. Coombs et al., 2004; le Roex et al., 2006). In this regard, it is relevant to note that while subsurface brines are likely to be rich in Cl and Sr, they are also likely to be depleted in uranium due to the predicted reduction of uranium from a +6 to an insoluble +4 oxidation state (e.g. Michard et al., 1983; Chen et al., 1986). A number of studies (e.g. Michard and Albarede, 1985; Chen et al., 1986; Ravizza et al., 2001; Ludwig et al., 2011) likewise found that U is effectively stripped out of ocean waters by hydrothermal activity. Rather than remaining in the brine, seawater-derived uranium and its radiogenic progeny should therefore be precipitated as secondary hydrothermal minerals in the crust. Any subsurface incorporation of these secondary mineral phases into the magma will significantly influence the concentrations of U and Th (Krolikowska-Ciaglo et al., 2007).

The ubiquitous, complex, and progressive post-eruptive alteration of basalt by seawater has likewise been well documented in studies including Macdougal et al. (1979), Staudigel et al. (1995), Stroncik and Schmincke (2002), and Krolikowska-Ciaglo et al. (2007), and others. These and other studies suggest multiple possible mechanisms by which fresh, uncontaminated mid-ocean ridge magmas can be subsequently altered by post-eruptive processes. Macdougall et al. (1979) observed scavenging of U from basalt upon interaction with seawater. They found that the concentrations and isotopic compositions of the measured uranium demonstrated a non-linear, continued interaction and exchange between seawater and the erupted basalts. Likewise, U addition can result from surface alteration of basaltic glass by seawater (Krolikowska-Ciaglo et al., 2007), but U concentration and ($^{234}U/^{238}U$) ratios do not appear related in a simple fashion (Glass et al., 2005; Sims et al., 2006). Bourdon et al. (2000) suggested that relatively altered (e.g. unpicked and/or unleached) MORB can develop elevated ($^{234}U/^{238}U$) ratios, $^{10}Be/^{9}Be$ ratios, ^{231}Pa excesses (e.g. Fig. 5), and, to a lesser extent, ^{230}Th excesses by interaction with seafloor sediments.

It has been further suggested, based on measurements of Cl in young glasses, that seawater vapor bubbles are sometimes incorporated into seafloor lava flows during emplacement (Soule et al., 2006). While one might expect this process to have a simple signal of wholesale seawater addition, given the complexities observed in volatile-glass fractionation and alteration during terrestrial eruptive and short-term post-eruptive processes (Moune et al., 2007), seawater–lava interaction during submarine eruptions is not likely to be so straightforward.

In Fig. 2, we show a calculated trajectory for simple seawater addition to an average of Kolbeinsey Ridge samples with ($^{234}U/^{238}U$) in equilibrium. A non-linear best-fit mixing curve of the data (dashed line; Sohn, 2005) and our calculated theoretical mixing trajectory (solid line) agree within the 95% confidence envelope for the non-linear fit. This similarity strongly supports the interpretation that Kolbeinsey Ridge lavas have been systematically affected by addition of seawater-derived materials.

In the Kolbeinsey Ridge samples, Cl/K_2O does not vary systematically with ($^{234}U/^{238}U$) (Fig. 6a), Th/U, or ($^{230}Th/^{238}U$) (not shown). Some Kolbeinsey samples demonstrate uniform Cl concentrations and Cl/K_2O ratios, while others show variations outside analytical uncertainty within a single glass chip, suggesting small-scale heterogeneity in the absorption of crustal material into the basalt (e.g. TRI0139-015-001G). The decoupling of Cl/K_2O from ($^{234}U/^{238}U$) observed in Fig. 6a is not surprising as there are a number of processes that can variably perturb Cl and/or U, such as Cl degassing (e.g. Carroll and Webster, 1994), assimilation of material with elevated K (e.g. celadonite), and/or assimilation of secondary high U concentration phases.

As summarized above, previous work has indicated that extensive surface alteration of basalt by seawater results in addition of U to altered glass (Krolikowska-Ciaglo et al., 2007) and a decrease in basaltic Th/U ratios (Verma, 1992; Soule et al., 2007). While the ($^{234}U/^{238}U$) ratios of our samples do not correlate with the U concentrations, which can be influenced by other processes, Kolbeinsey Ridge ($^{234}U/^{238}U$) does correlate with Th/U ratios (Fig. 6b). This initially appears consistent with results for alteration, which may involve a complex exchange of U between seawater-derived components and MORB glass such that ($^{234}U/^{238}U$) does not always correlate with U concentration (Glass et al., 2005; Sims et al., 2006).

$^{87}Sr/^{86}Sr$ and Sr concentrations also do not vary systematically with Kolbeinsey Ridge ($^{234}U/^{238}U$) (Fig. 6). However, because the concentrations of U in seawater are relatively high, interaction with secondary hydrothermal mineral deposits or seawater should dramatically perturb the U-series system and may have less of an effect on Sr isotopes (Sims et al., 2003). This is illustrated in Fig. 6, which shows that the direct addition of U from seawater, with a seawater/rock ratio of 0.9 by weight, would perturb a Kolbeinsey glass with initial U concentration of 0.028 ppm and ($^{234}U/^{238}U$) = 1.000 to an altered ($^{234}U/^{238}U$) ratio of 1.014, with negligible effect on the Sr isotope compositions. A simple mixing calculation between seawater and average, unaltered Kolbeinsey basalt (with 86 ppm Sr, $^{87}Sr/^{86}Sr = 0.70291$, 0.11 ppm U, and ($^{234}U/^{238}U$) = 1.000), however, does not follow the trajectory of the Kolbeinsey data, which suggests addition of an enriched crustal component that is much higher in uranium content than seawater (e.g. hydrothermal deposits with U rich minerals), i.e. a crustal contamination signature rather than post-eruptive alteration. For example, a basalt plus seawater mixture generates a ($^{86}Sr_{seawater} \times {}^{238}U_{Kolbeinsey\ MORB}$)/($^{86}Sr_{Kolbeinsey\ MORB} {}^{238}U_{seawater}$) mixing ratio equal to 3.2, which produces the wrong sense of hyperbolic curvature in Fig. 6c, whereas a hypothetical enriched crustal component with 100× more U and a similar ($^{234}U/^{238}U$) ratio to seawater generates a mixing ratio of 0.03 and more closely follows the data trajectory. In fact, this uranium enriched hypothetical component can explain the most altered Kolbeinsey sample by addition of only 8–10% crustal material to the unaltered basalt, rather than the more problematic ~1:1 water:rock ratio suggested by a pure seawater component as the U-isotope contaminant. Based on the discussion above, we expect such a contaminant to most likely comprise hydrothermally altered crustal rocks.

However, as described above, our electron probe data (Fig. 6a) demonstrate that no single, simple mechanism, such as subsurface assimilation of hydrothermally altered rocks, can explain both the Cl/K_2O ratios and the ^{238}U-^{230}Th isotopic relationships we observe. Due to the complex speciation and solubility of U under various redox conditions (Mitchell, 1993), it is difficult to precisely predict the behavior of U in the crust. It follows from the discussion above, however, that Cl could be mainly added by seawater brines (Michael and Cornell, 1998) (Fig. 7a), while U is added by the absorption of altered rocks (Fig. 6c). As has been recently noted for Loihi submarine basalts, variations of ($^{234}U/^{238}U$) with basalt chemistries also require multiple decoupled processes, including variable absorption of both brines and secondary hydrothermal mineralization in the crust (Pietruszka et al., 2011).

5.3. Assessing primary $^{230}Th/^{238}U$ of Kolbeinsey Ridge basalts

The best estimate of the ($^{230}Th/^{238}U$) ratio of Kolbeinsey Ridge basalts is from the samples with ($^{234}U/^{238}U$) in equilibrium. The Kolbeinsey Ridge samples with $^{234}U/^{238}U = 1.000 \pm 0.005$ have ($^{230}Th/^{238}U$) = 1.19 to 1.30.

A second, but less certain estimate of the primary ($^{230}Th/^{238}U$) of Kolbeinsey Ridge melts for altered samples is to approximate a linear trajectory of alteration based on the overall best-fit trend for the data set. In Table 2 we calculate uncontaminated ($^{230}Th/^{238}U)_c$ values using the best fit slope, correcting to a ($^{234}U/^{238}U$) value of 1.0; with this approach, calculated ($^{230}Th/^{238}U)_c = 1.15$–$1.33$. While the most robust data are those with ($^{234}U/^{238}U$) in equilibrium, it is noteworthy that corrected altered samples exhibit a similar range in ($^{230}Th/^{238}U$) as is measured in the seemingly unaltered samples. Thus, all indications are that Kolbeinsey MORB have ($^{230}Th/^{238}U$) values ranging from 1.15 to 1.30 prior to eruption, and that the samples with ($^{230}Th/^{238}U$) < 1 result from shallow crustal modification. These Kolbeinsey data clearly illustrate the need for robust measurement of ($^{234}U/^{238}U$) in MORB, and for caution in interpreting the ^{238}U–^{230}Th disequilibria measured in samples that contain ($^{234}U/^{238}U$) out of secular equilibrium (e.g. Tepley et al., 2004).

5.4. Uranium-series constraints on melting beneath the Kolbeinsey Ridge

The high ($^{230}Th/^{238}U$) (1.19 to 1.30) and ($^{231}Pa/^{235}U$) values (1.22 to 2.50) of Kolbeinsey Ridge basalts with

($^{234}U/^{238}U$) in equilibrium place important constraints on the melting processes occurring beneath this ridge. Melting calculations using a forward modeling approach for ^{238}U–^{230}Th and ^{235}U–^{231}Pa are presented below and in Figs. 8–10.

The Kolbeinsey Ridge lavas show evidence for an isotopically homogeneous source, within analytical uncertainties, along most of the ridge length (from 67.0°N to 70.7°N), with the exception of a few samples very close to Iceland on the leaky Tjörnes Fracture Zone (south of 67°N) and near the Jan Mayen Fracture Zone (north of 70.7°N), where lavas are more isotopically enriched (Fig. 3) (Mertz et al., 1991; Mertz and Haase, 1997; Schilling et al., 1999; Haase et al., 2003; Blichert-Toft et al., 2005). Unaltered Kolbeinsey samples between 67.0°N and 70.7°N have universally large ^{230}Th excesses, and the nearly uniform Nd, Sr, Hf, and Pb isotopic compositions suggest a relatively homogenous source over the length scale of melting.

Due to the shallow ridge axis, thick crust, high degree of melting, and proximity to the Iceland melting anomaly, Kolbeinsey Ridge melts are likely derived from a deep, long melting column that samples both garnet-bearing (i.e. garnet peridotite) and garnet-free (spinel peridotite) lithologies along its length (Bourdon et al., 1996a; Klein and Langmuir, 1987). Bourdon et al. (1996a) have shown that on a global scale there is a broad negative correlation between the magnitude of ^{238}U–^{230}Th disequilibrium and the axial ridge depth of MORB. Their interpretation, based on the petrogenetic interpretations of Klein and Langmuir (1987), was that this correlation reflects mantle temperature variations beneath the ridge: hotter mantle intersects its solidus at a greater depth, resulting in a longer melt column and more melt generation, which in turn generates thicker crust, a shallower ridge, and larger ^{230}Th excess (because of the longer melt column in the garnet stability field). Bourdon et al. (1996a), thus, predicted that shallow ridges with thick crust such as the Kolbeinsey Ridge should have the highest ^{230}Th excesses, reflecting strong garnet signatures. Russo et al. (2009) and others, however, have argued that the observed correlation is weak, particularly as additional data have become available, and that this temperature-dependent scenario may only apply in a very general way to global data and thus neglects potentially important influences from other factors, including melting more fertile mantle lithologies, which would produce greater quantities of melt and, by extension, thicker crust (e.g. Langmuir et al., 1992; Shen and Forsyth, 1995; Niu and Batiza, 1997; Russo et al., 2009). An important, first-order result of our study is that the high ($^{230}Th/^{238}U$) of the shallow Kolbeinsey Ridge basalts fit the predictions of Bourdon et al. (1996a). Coupled with other geochemical constraints, namely that the Kolbeinsey Ridge basalts have highly depleted major and trace element compositions and are isotopically relatively uniform (which means the source is relatively homogeneous over the length scale of melting), the above observation strongly supports the hypothesis that on a global scale, axial ridge depth is dominantly controlled by mantle temperature effects on solidus depth and melt supply.

5.4.1. Forward modeling of the U-series data: overview

In general, melting processes during basalt petrogenesis can generate both U-Th elemental fractionation (Gill et al., 1990; Sims et al., 1995, 1999; Elliott, 1997; Condomines and Sigmarsson, 2000; Green et al., 2001; Sims and Hart, 2006) and ^{230}Th ingrowth from parent ^{238}U due to the effects of time on melting and melt transport (Mckenzie, 1985; Williams and Gill, 1989; Spiegelman and Elliott, 1993; Elliott, 1997; Sims et al., 1999, 2002). Slow upwelling beneath a slow spreading ridge makes ^{230}Th ingrowth an important process, particularly in the generation of large ^{230}Th excesses in basalts that are interpreted as products of high degrees of melting. Clearly, simple time-independent calculations of melting (e.g. batch melting) cannot explain the entirety of Kolbeinsey Ridge data; with simple batch and/or fractional melting the large ^{230}Th excess would require small degrees of melting (generally $<1\%$ melting; e.g. Sims et al., 1995), whereas estimated degrees of melting for the Kolbeinsey Ridge from major element chemistry (Na_8 and Ca/Al_8) and trace element ratio depletions predict melt fractions of 11–28% (Schilling et al., 1999).

Thus we consider more complicated melting scenarios that incorporate the effects of daughter nuclide ingrowth for the Kolbeinsey samples: ingrowth models allow for larger overall melt fractions while maintaining significant parent-daughter fractionation. Below, we use dynamic and reactive porous flow 1D forward melting models to evaluate Kolbeinsey Ridge ^{238}U–^{230}Th and ^{235}U–^{231}Pa disequilibria in the context of the major and trace element compositions of the samples analyzed here.

5.4.2. Constraints on Kolbeinsey basalt genesis from ^{238}U–^{230}Th disequilibria

The large ^{230}Th excesses of the Kolbeinsey lavas favor a long melt column that initiates in the garnet stability field and generates the deep melting (Fe_8) and high melt fraction signatures observed in the major elements of the lavas. Using both dynamic and reactive porous flow time-dependent melting calculations, we calculate melt trajectories for a peridotite source (Fig. 8).

Since lavas from most of the length of the Kolbeinsey Ridge have relatively homogeneous ($^{230}Th/^{238}U$), as well as radiogenic isotopes and trace element ratios, it is straightforward to use a 1-D forward melting model to determine the conditions under which such lavas could be produced. As explained above, the Kolbeinsey Ridge overlies thick crust (implying large degrees of melt) and produces lavas with high ($^{230}Th/^{238}U$) ratios, indicating that residual garnet in their source is required. One-dimensional dynamic and equilibrium porous flow models with constant melt productivities and partition coefficients are expected to work well for modeling a single average melt composition, which is essentially what the Kolbeinsey Ridge lavas become after removing the effects of secondary processes (see Section 5.1).

Since these simpler models adequately explain the Kolbeinsey Ridge melt compositions, we limit our calculations to modal melts with constant melt productivities and partition coefficients (e.g. Mckenzie, 1985; Bourdon et al., 1996a; Lundstrom, 2000; Spiegelman, 2000; Jull et al.,

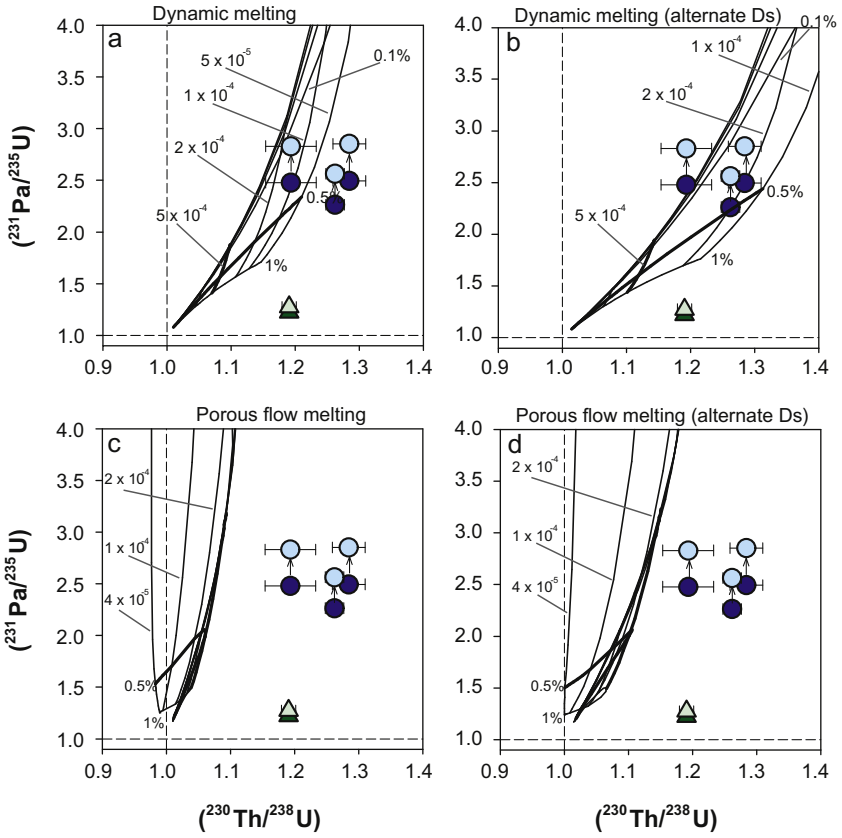

Fig. 8. Results of (a and b) dynamic and (c and d) reactive porous flow calculations for melting of garnet peridotite over a range of melting rate (M) and residual porosity (φ) inputs. All results shown reflect the calculated final melt composition at the top of the melt column. Melt calculations further explained in the text and Table 4; symbols as in Fig. 5 (only samples with measured ($^{234}U/^{238}U$) in equilibrium are shown). Lighter shaded circles and triangles show maximum ($^{231}Pa/^{235}U$) values for Kolbeinsey Ridge samples as though they are 10,000 years old (Table 2). Except for the sample from the Eggvin Bank (green triangle), most Kolbeinsey MORB can be reproduced by both sets of calculations. The melts in (a) and (c) were calculated using the partition coefficients in Table 4, while the melts shown in (b) and (d) are calculated for slightly different partition coefficients, as explained in the text, and demonstrate the sensitivity of model calculations to small changes in partitioning behavior. Curves are shown for melts with variable porosities and constant melting rates of 5×10^{-3}, 1×10^{-3}, 5×10^{-4}, 2×10^{-4}, 1×10^{-4}, and 4×10^{-5} kg/m^3/yr, and for variable melting rates and constant porosities of 1%, 0.5%, 0.1%, 0.05%, 0.03%, and 0.02%. Since UserCalc requires an input of the solid upwelling rate instead of the melting rate, we calculate a solid upwelling rate from the mean melting rate desired using the equation $M = W\rho_s F_{max}/d$, where M is the mean melting rate, W is the solid upwelling rate, ρ_s is the solid density (3300 kg/m^3), F_{max} is the maximum degree of melting, and d is the length of the melt column. Lines in bold are for reference and indicate a constant melting rate of 5×10^{-4} kg/m^3/yr and a constant porosity of 0.5%.

2002). This is a reasonable approximation given the inherent limitations produced by uncertainties in mineral/melt partition coefficients (see below). With dynamic melting, ^{238}U–^{230}Th disequilibrium is produced at the bottom of the melt column, whereas during reactive porous flow melting rock interaction is continuous. We thus use a simple garnet lherzolite melt column for dynamic melting, but we impose a two-layer mantle model (garnet lherzolite overlain by spinel lherzolite) on the reactive porous flow melt model. The results of our calculations show that the reactive flow model is sensitive to the imposed heterogeneity in partition coefficients along the melt column, such that the phase change from spinel to garnet peridotite has a significant impact on U and Th partitioning behavior during melting (e.g. Spiegelman and Elliott, 1993).

In all of our melting calculations, the mantle source is assumed to be in secular equilibrium, which is reasonable given the age of the mantle source beneath the Kolbeinsey Ridge relative to the half-lives of the relevant nuclides. We chose a peridotite source with initial ($^{238}U/^{232}Th$) = ($^{230}Th/^{232}Th$) = 1.25 to best generate melt compositions near the average Kolbeinsey Ridge ($^{230}Th/^{232}Th$) value. This is considerably lower than the Depleted MORB Mantle (DMM) U/Th range of 0.50–0.53 regressed by Sims and Hart (2006), but is reasonable for a source postulated to represent a mixture between DMM and FOZO, as suggested by the long-lived Nd, Sr, Pb, and Hf isotopic data (Blichert-Toft et al., 2005; Sims and Hart, 2006). We calculate aggregate melts for a 100 km peridotite melting column that initiates in the garnet peridotite stability field. In such a long melting column, the presence of garnet generates large ^{230}Th-excesses in the deepest melts. In the absence of garnet (or some clinopyroxene compositions that can also produce moderate ^{230}Th excess (e.g. ~20%; Wood et al., 1999; Land-

Table 4
Mineral/melt partition coefficients and initial mineral modes for our melting model calculations.[a] $D_{Pa} = 1 \times 10^{-5}$ for all models.

	Mineral/melt partition coefficient D_i					Mineral mode[d]
	U	Th	Sm	Nd	La	
Garnet peridotite[b]						
Garnet	0.038	0.017	0.22	0.074	0.0010	0.12
Clinopyroxene	0.0030	0.0040	0.093	0.072	0.054	0.08
Olivine	0.00005	0.00047	0.0013	0.0010	0.00001	0.59
Orthopyroxene	0.0078	0.0086	0.029	0.021	0.0010	0.21
Bulk	0.0065	0.0044	0.041	0.020	0.0046	
Spinel peridotite[b]						
Clinopyroxene	0.0080	0.0070	0.319	0.186	0.0536	0.2
Olivine	0.0001	0.0005	0.001	0.001	0.0000	0.6
Orthopyroxene	0.0024	0.0027	0.016	0.010	0.0010	0.2
Bulk			0.029			
Eclogite[c]						
Garnet	0.024	0.00415	0.363	0.29	0.00425	0.4
Clinopyroxene	0.0041	0.0032	0.19	0.122	0.027	0.6
Bulk	0.012	0.0036	0.26	0.19	0.018	

We assume peridotite solidus depths of 100 km and an eclogite solidus 25 km deeper than the peridotite solidus.
The peridotite melting interval is 450 °C, while the eclogite melting interval is 100 °C (where "melting interval" refers to the temperature difference between the liquidus and the solidus). We assume a solid mantle density of 3300 kg/m^3 and a melt density of 2800 kg/m^3.
[a] Peridotite melting calculations assume a U_0 (initial U concentration) of 0.0018 ppm, Th_0 of 0.00071, and Pa_0 of 5.81×10^{-7} ppb.
[b] Partition coefficients from Kelemen et al. (1997), Salters and Longhi (1999), Salters et al. (2002).
[c] Partition coefficients from Pertermann et al. (2004).
[d] Mineral modes for lithologies described in the text.

wehr et al., 2001)), fractionation is mainly controlled by clinopyroxene with $D_{Th} > D_U$, creating small ^{238}U excesses in the melt (La Tourette and Burnett, 1992; La Tourette et al., 1993; Beattie, 1993a,b; Hauri et al., 1994; Lundstrom et al., 1994; Salters and Longhi, 1999; Wood et al., 1999; Landwehr et al., 2001; Salters et al., 2002; Elkins et al., 2008).

For our forward models, we vary the melting rates between 4×10^{-5} and 5×10^{-3} kg/m^3/yr and the porosities between 0.02% and 1%. We approximate solid upwelling rates using the basic relationship, $M = W\rho_s F_{max}/d$, where M is the mean melting rate, W is the solid upwelling rate, ρ_s is the density of the solid mantle, F_{max} is the maximum extent of melting, and d is the length of the melt column. Although the mean melt rate and melting constant of Zou and Zindler (2000) diverge at slow melting rates, the melting rates tested nonetheless approximately correspond to a broad range of solid upwelling rates between 0.6 and 75 cm/yr, assuming a maximum of 20% melting over a 100 km column (for reference, the half-spreading rate for the Kolbeinsey Ridge is 9 mm/yr; Mosar et al., 2002). We assume a two-layer mantle model for reactive porous flow melting and use uniform partition coefficients for garnet peridotite above 2.5 GPa and for spinel peridotite at shallower depths. For the reactive porous flow model, calculations are performed using UserCalc (Spiegelman, 2000), which works from incremental inputs for depth of melting, degree of melting, and partition coefficients to calculate continuous variations in melt composition in a 1-D upwelling mantle column. We calculate dynamic melts using the formulae described in Zou and Zindler (2000). We place constraints on each model run by limiting solid upwelling rates and corresponding mean melt rates, maximum residual melt porosities, the depth of the peridotite solidi, and the bulk partition coefficients for each lithology, as explained further below.

^{238}U–^{230}Th disequilibrium results for a series of progressive melting scenarios (dynamic and porous flow) are shown in Fig. 8 (partition coefficients as in Table 4). As expected, at typical melting conditions for a slow-spreading ridge (0.5% maximum porosity and a solid upwelling rate of 1 cm/year), accumulated high-degree porous flow melts from the top of the melt column do not preserve large ^{230}Th excesses generated deeper in the column, due to reequilibration with garnet-free rocks.

Any successful melting model for the Kolbeinsey Ridge needs to reproduce the following constraints: (1) depleted in trace elements relative to most MORB, which infers high F; (2) high ($^{230}Th/^{238}U$), which infers a deep garnet signature; and (3) uniform in radiogenic isotopes, which infers that the source is chemically and lithologically homogeneous over the length scale of melting. While the dynamic melts can maintain large ^{230}Th excesses to degrees of melting above 10%, the reactive porous flow melts can only do so deep in the melt column (not shown). Reactive flow melts extracted from those depths correspond to melt fractions of 4–5% or less, which are thought too low to explain the major and trace elements (e.g. Na_8) or the thick crust observed.

A concern regarding the reactive porous flow model is the long melt column, within which the reacting melt travels through the garnet-spinel transition. The model results described above suggest that a dynamic melting model can account for the Kolbeinsey Ridge data because the majority of the ($^{230}Th/^{238}U$) disequilibria is generated during the ini-

tiation of melting, after which the peridotite source is too depleted in U and Th to significantly modify the melt composition. However, for a 1D reactive porous flow model the spinel peridotite signal obscures the ^{230}Th excesses initially produced in the deeper, garnet peridotite portion of the column. An alternate explanation for the discrepancies between the reactive flow forward melting results and the Kolbeinsey basalts is that the Kolbeinsey melt regime is a "two-porosity" system, similar to those previously suggested to be important in generating the inverse correlations between ^{226}Ra and ^{230}Th excesses in EPR basalts (e.g. Iwamori, 1994; Kelemen et al., 1997; Lundstrom, 2000; Jull et al., 2002; Sims et al., 2002; Waters et al., 2011). We would predict the high-(^{230}Th/^{238}U) basalts from the Kolbeinsey Ridge to have low (^{226}Ra/^{230}Th) in such a scenario; however, while our measured sample does have a low ^{226}Ra excess, without age constraints it is impossible to tell if the measured (^{226}Ra/^{230}Th) ratio reflects a deep, low-degree melt along the ^{230}Th–^{226}Ra inverse correlation, or if it is the product of aging. A straightforward mixing calculation suggests that such mixtures cannot produce both the high (^{230}Th/^{238}U) ratios observed and sufficiently high degrees of melting in the same melts, but since such a mixing model requires age-constrained ^{230}Th–^{226}Ra data we cannot robustly constrain such a model for the Kolbeinsey Ridge.

5.4.3. Constraints on Kolbeinsey basalt genesis from ^{235}U–^{231}Pa disequilibria

Fig. 5 and Table 2 show that (^{231}Pa/^{235}U) ratios for the Kolbeinsey Ridge south of 70.7°N average 2.41, while the more isotopically and trace element enriched sample north of 70.7°N has lower (^{231}Pa/^{235}U) = 1.22, more closely resembling OIB compositions (see e.g. Sims et al. (2008a) for compilation of (^{231}Pa/^{235}U) and (^{230}Th/^{238}U) in MORB and OIB). Table 2 also presents age-corrected (^{231}Pa/^{235}U) ratios for these samples, assuming they are the maximum possible age of 10,000 years. These age corrected (^{231}Pa/^{235}U)$_{max}$ values (Table 2 and Fig. 5) thus represent the maximum possible (^{231}Pa/^{235}U) ratios upon eruption for these samples.

The ^{235}U–^{231}Pa system is particularly sensitive to shorter-lived processes than ^{238}U–^{230}Th due to the comparably short half-life of ^{231}Pa (half-life of 3.2 ka; Robert et al., 1969). Unlike the ^{238}U–^{230}Th system, in which the relative partitioning behavior of U and Th is extremely sensitive to the presence or absence of garnet, Pa is always much more incompatible than U in all mantle phases; however, due to the shorter half-life, ^{235}U–^{231}Pa disequilibria are not preserved as well as ^{238}U–^{230}Th disequilibria during upwelling after melt extraction.

(^{231}Pa/^{235}U) results for the dynamic and reactive porous flow melt calculations described above are combined to produce the melting grids shown in Fig. 8. The models calculate (^{231}Pa/^{234}U) and (^{230}Th/^{238}U) ratios at the top of the 100 km melt column, as a function of residual porosity (with constant mean melting rate) or mean melting rate (with constant porosity). Some, but not all of these model runs produce results within uncertainty of the measured Kolbeinsey data, with the exception of the basalt from the Eggvin Bank segment. The dynamic melt calculations suggest a range of conditions that can produce the range of Kolbeinsey MORB, from one set of parameters where mean melt rates are high (2×10^{-4} kg/m^3/yr, or 3 cm/yr solid upwelling rate) and residual melt porosities are very low (0.2%), to another with lower mean melting rates (4×10^{-5} kg/m^3/yr, or 0.6 cm/yr solid upwelling rate) and higher porosities (0.5%). The range of predicted solid upwelling rates bracket the 0.9 cm/yr half-spreading rate observed at the Kolbeinsey Ridge, suggesting upwelling rates are similar to the rate of plate spreading along the ridge. Reactive porous flow calculations, on the other hand, do not easily reproduce Kolbeinsey melt compositions because of chemical reequilibration with spinel peridotite at depths shallower than 2.5 GPa.

As demonstrated in e.g. Elkins et al. (2008) and Stracke et al. (2006), there are relatively large deviations across experimental measurements of mineral/melt partitioning for U and Th that translate into a high degree of uncertainty in the resulting calculated parameters (e.g. Sims et al., 1999). Fig. 8 highlights how calculated melt compositions are highly sensitive to the partition coefficients selected. After rounding the bulk partition coefficients of D_U from 0.0065 to 0.007 and D_{Th} from 0.0044 to 0.004, the ability of the melting models to reproduce the Kolbeinsey Ridge data, and the predicted conditions under which those melts might be generated, change significantly, particularly for dynamic melts. Thus, limitations in our knowledge of the partition coefficients from experiments and theoretical calculations, and how those values vary during progressive melting in an upwelling column, limit our ability to precisely determine the fundamental parameters of melting (i.e. porosity, mantle upwelling rates, melt dispersity, etc.).

In general, Kolbeinsey basalts have relatively high (^{230}Th/^{238}U) for global MORB range and low (^{230}Th/^{238}U) compared to the range of Icelandic lavas. With the exception of the unaltered sample from the Eggvin Bank, Kolbeinsey Ridge basalts resemble global MORB in that their (^{231}Pa/^{235}U) ratios are considerably higher than those of OIB (Fig. 5, and references therein). Fig. 8a–d demonstrates that higher (^{230}Th/^{238}U) at a given (^{231}Pa/^{235}U) can be achieved by (1) switching from a reactive porous flow to a dynamic melting model, i.e. by more efficient disequilibrium melt extraction (this is due to the sensitivity of porous flow melts to the disappearance of garnet during ascent in a peridotitic melt column), (2) increasing from low to intermediate melt rates for reactive porous flow melts and, conversely, by decreasing melt rate for dynamic melts; or (3) decreasing residual melt porosity.

We note that none of our peridotite melting calculations pass through the extremely low (^{231}Pa/^{235}U) ratio measured in the sample from the Eggvin Bank, despite considering a wide range of melting rates and maximum residual porosity conditions. The low (^{231}Pa/^{235}U) ratio argues against shallow assimilation or melt–rock reaction as a source of enriched trace element signatures, which would cause higher, not lower ^{231}Pa excesses (e.g. Bourdon et al., 2000). A second possible explanation, which the models shown in Fig. 8 do not consider, is lithologic heterogeneity in the melt source region. Although the relative homogene-

ity in radiogenic isotopic composition of most Kolbeinsey Ridge basalts argued against a heterogeneous mantle source control in our discussion above, consideration of the Eggvin Bank lavas, with their isotopically enriched compositions, suggests that mantle source lithologic variation may in fact influence the generation of melts along the northernmost ridge segment. Previous studies have argued that source heterogeneity, in addition to mantle temperature, exerts an important control over variations in global MORB geochemistry (e.g. Niu and Batiza, 1993, 1997; Niu et al., 2001; Russo et al., 2009; Waters et al., 2011). In particular, the presence of small amounts of garnet-bearing eclogite in the mantle source could potentially produce melts with lower (^{231}Pa/^{235}U) ratios than peridotite, due to the presence of garnet at shallow depths and higher degrees of melting predicted for eclogite (Hirschmann and Stolper, 1996; Pertermann and Hirschmann, 2003; Waters et al., 2011). We would expect a second, more fertile lithology, such as eclogite, to have a deeper solidus and higher melt productivity than peridotite, which would be enhanced by superadiabatic heating through heat exchange from ambient subsolidus material during melting (Hirschmann and Stolper, 1996; Pertermann and Hirschmann, 2003). The larger degrees of melting that would result from melting a secondary lithology are expected to reduce the (^{231}Pa/^{235}U) ratios in the melts produced, which, when mixed with the more voluminous peridotite melts produced higher in the melt column, could lower the overall ^{231}Pa excesses observed.

In Fig. 9 we show the results of dynamic and reactive porous flow melting for an eclogite source (Table 4) over a melting interval of 100 °C, such that the eclogite is exhausted after approximately 30 km of melting. Although none of the calculated melt compositions pass directly through our data, the dynamic melt compositions shown are considerably closer to the composition of the basalt sampled on the Eggvin Bank than our previous models (Fig. 8). The reactive porous flow melts, on the other hand, are a poor fit for any of our data; this is not surprising, since melts of minor lithologies with deeper solidi than peridotite must experience efficient, disequilibrium extraction to avoid freezing upon reaction with ambient peridotite rock. Considering predictions by Hirschmann and Stolper (1996) and Kogiso et al. (2004), and others, expected melting rates for eclogite rocks might be even higher than our calculations, likely resulting in melts with even lower (^{230}Th/^{238}U) and (^{231}Pa/^{235}U) compositions than those shown. MORB from the Eggvin Bank do contain, on

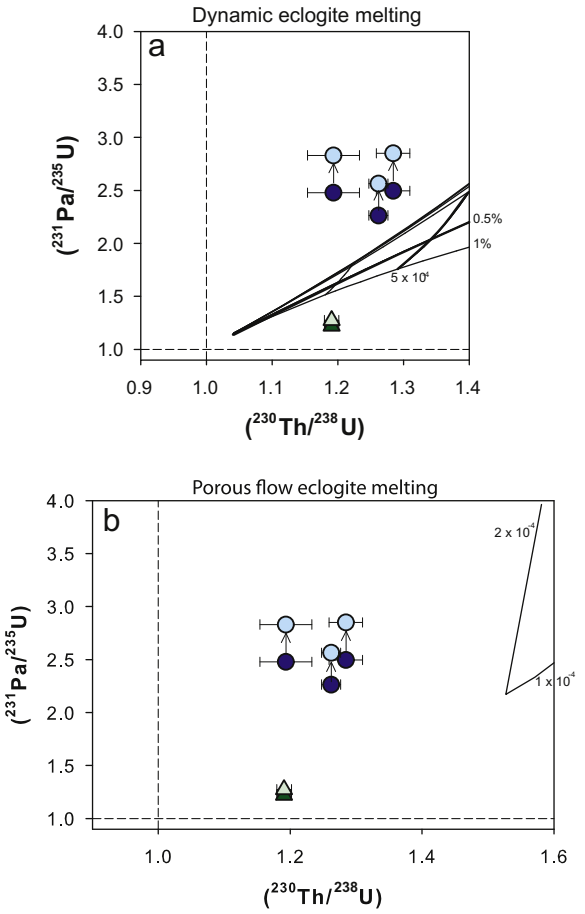

Fig. 9. Results of eclogite melting calculations, as explained in the text and Table 4. Panels show the compositions of (a) dynamic and (b) reactive porous flow melts at the top of the melting columns, as in Fig. 8. Data symbols and line weights as in Fig. 8, except that melt rates of 4×10^{-5} kg/m^3/yr are not shown, due to the extremely slow upwelling rates implied for a lithology with such a narrow melting interval (100 °C).

Table 5
Calculated α_{Sm-Nd} values for samples in this study.

Sample	Location	α_{Sm-Nd}[a]
TRI0139-001-001G	Tjörnes FZ	1.233
POS185 1105B	Tjörnes FZ	1.155
POS185 1093	S. Kolbeinsey	1.082
POS291 485-3	S. Kolbeinsey	1.088
TRI0139-007-001G	S. Kolbeinsey	0.983
POS326 540DS-4	S. Kolbeinsey	1.035
POS291 495-2	S. Kolbeinsey	1.053
POS185 1096A	S. Kolbeinsey	0.966
POS185 1094B	S. Kolbeinsey	1.024
TRI0139-006-002G	S. Kolbeinsey	1.037
TRI0139-013-003G	S. Kolbeinsey	1.045
TRI0139-014-001G	S. Kolbeinsey	0.998
TRI0139-015-001G	S. Kolbeinsey	1.058
TRI0139-016-001G	S. Kolbeinsey	1.028
POS0002/2 Geo 212	S. Kolbeinsey	0.999
TRI0139-020-001G	S. Kolbeinsey	0.911
POS221 596DS-1	S. Kolbeinsey	0.895
POS221 605DS-2	S. Kolbeinsey	1.011
POS210/1 682DS-1	N. Kolbeinsey	0.947
POLARK7-1-21844	N. Kolbeinsey	1.081
POLARK7-1-21847	N. Kolbeinsey	1.216
POLARK7-1-21848	N. Kolbeinsey	1.103
POLARK7-1-21850	N. Kolbeinsey	1.236
POLARK7-1-21854	N. Kolbeinsey	1.185
POS210/1 700 DS-2	Eggvin Bank	0.799
POS210/1 702 DS-1	Eggvin Bank	0.924
POS210/1 698 DS-1	Eggvin Bank	0.739
TRI0139-027-005G	Eggvin Bank	0.667

[a] $\alpha_{Sm-Nd} = (Sm/Nd)_{sample}/(Sm/Nd)_{source}$, where $(Sm/Nd)_{source}$ is derived from the measured ε_{Nd} value of the sample and a model age of 1.8 Ga.

average, slightly higher SiO_2 (51% vs. 50%) contents than other Kolbeinsey Ridge basalts, and, more notably, considerably higher La/Sm_N ratios (1.83 and 0.51, respectively), Sm/Yb_N ratios (1.08 vs. 0.84), and La/Yb_N ratios (1.92 vs. 0.41). These trace element ratios would be inconsistent with a high degree of melting if the source compositions for the two regions were the same, but since high Th/U ratios may indicate a more trace element-enriched source for the Eggvin Bank, we consider these ratios to reflect a relatively enriched, possibly eclogite-bearing source beneath the Eggvin Bank ridge segment.

Eclogite is predicted to be a minor mantle lithology (~5%; Hirschmann and Stolper, 1996). However, it is possible that eclogite melts are more readily directly sampled in regions that experience slow upwelling and overall lower degrees of melting (e.g. the Eggvin Bank), and where the eclogite signature, hence, is less overwhelmed by subsequent melting of the dominantly peridotitic mantle above the peridotite solidus. The presence of a basalt with a very low measured ($^{231}Pa/^{235}U$) value on the Eggvin Bank, which is thought to overlie thin to normal crust over a more buoyant and heterogeneous mantle (Schilling et al., 1999; Tronnes et al., 1999; Haase et al., 2003; Mertz et al., 2004; Blichert-Toft et al., 2005), may reflect such a process of eclogite melt sampling at depth. In other parts of the Kolbeinsey Ridge, such extremely low ($^{231}Pa/^{235}U$) signatures are not observed, and the samples are more easily explained as melts of peridotite. This distinction demonstrates the value of a combined approach, looking at both ^{238}U–^{230}Th and ^{231}Pa–^{235}U systematics when evaluating MORB melting scenarios.

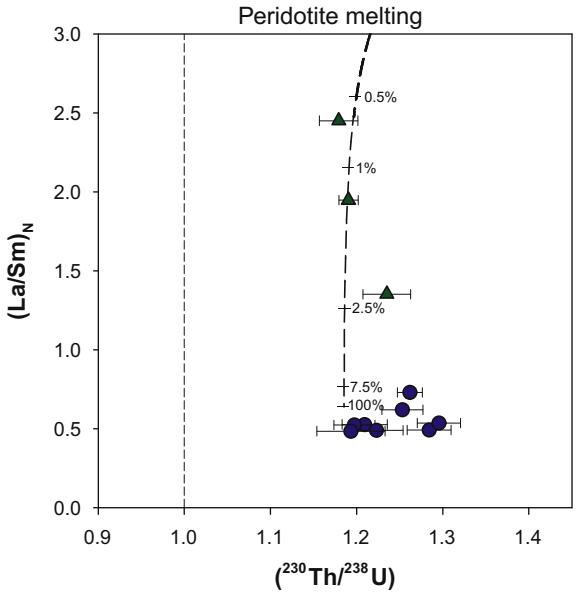

Fig. 10. Dynamic (dashed line) melt trajectory for a single progressive melting column with a melting rate of 7×10^{-5} kg/m^3/yr and a maximum porosity of 0.5%, plotted for La/Sm_N vs. ($^{230}Th/^{238}U$). Tick marks and tick mark labels indicate the progressive degree of melting along the melt column. Symbols as in Fig. 8.

5.5. Nature of the Kolbeinsey source: radiogenic isotope age models and trace element fractionation

While it is possible to produce coupled large ^{230}Th and ^{231}Pa excesses with these melting models, the Sm/Nd trace element systematics are problematic. Salters (1996) observed that α_{Sm-Nd} values, which quantify the relationship between the Sm/Nd ratio of a melt and that of its postulated source composition, are anomalously high in Kolbeinsey lavas (i.e. $\alpha_{Sm-Nd} = (Sm/Nd)_{sample}/(Sm/Nd)_{source}$, where

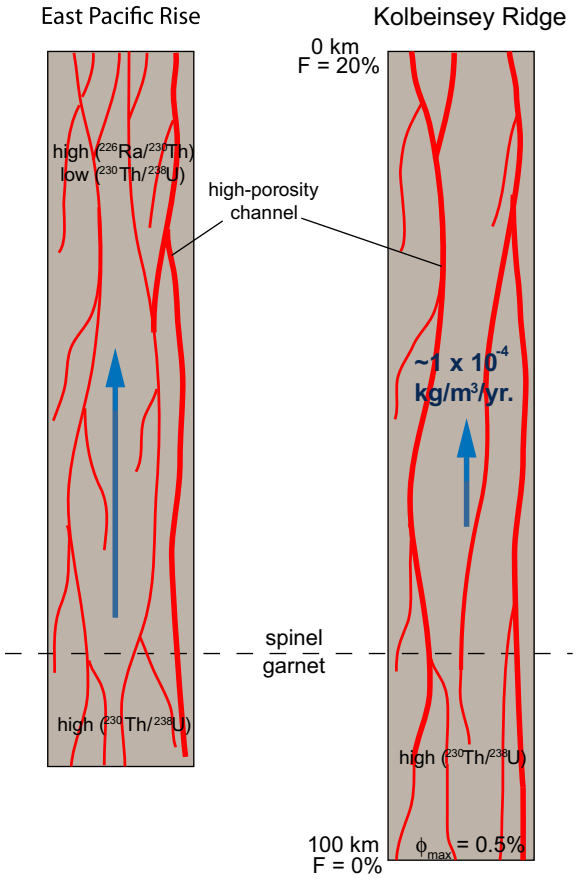

Fig. 11. Schematic one-dimensional diagrams comparing melting beneath the EPR (after Sims et al. (2002)) and the Kolbeinsey Ridge. On the EPR, melting begins in the garnet peridotite stability zone, generating melts with large ^{230}Th excesses. The Kolbeinsey Ridge peridotite solidus is deeper than the solidus for the EPR, reflecting the hot mantle adjacent to Iceland and the higher degrees of melting necessary to generate the thick crust and Kolbeinsey MORB chemical abundances. The Kolbeinsey melt column contains recently depleted source rock compared to average MORB-source mantle. The relative sizes of the arrows denote the very different passive upwelling rates predicted by the spreading rates of the two ridges (where the Kolbeinsey Ridge spreads much slower than the fast-spreading EPR). On the EPR, in particular, shallow interaction of melts in low-porosity zones with depleted residual rocks near the top of the melt column produces shallow melts with high ($^{226}Ra/^{230}Th$), while deeper melts moving in faster, disequilibrium channels preserve the large ^{230}Th excesses from deep. Low ($^{230}Th/^{238}U$) melts are not seen at the Kolbeinsey Ridge, possibly because they are not extracted and sampled through the thicker overlying crust.

$(Sm/Nd)_{source}$ is calculated from each sample's ε_{Nd} value using a model age of 1.8 Ga (DePaolo, 1988; Sims et al., 1995)). The α_{Sm-Nd} values for the Kolbeinsey Ridge lavas sampled in this study range from 0.91 to 1.24 and are almost all greater than one (Table 5), in agreement with Salters (1996). Salters and Hart (1989) examined the importance of garnet in producing the Lu–Hf and Sm–Nd relationships in Kolbeinsey Ridge basalts and found that a 500 Ma mantle source can explain better the Kolbeinsey MORB than an assumed 1.8 Ga mantle age.

Other trace element ratios (e.g. chondrite-normalized La/Sm_N) are also depleted for Kolbeinsey Ridge basalts (Fig. 10), but these likewise can be reasonably well explained by melting of a peridotite source (Section 5.2). The modeled melt trajectory in Fig. 10 shows variations with progressive degree of dynamic melting in a single upwelling column, assuming an initial source rare-earth element composition based on the DMM component from Workman and Hart (2005).

5.6. MORB generation beneath the Kolbeinsey Ridge

To a first order, our model calculations show that Kolbeinsey major and trace element, isotopic, and U-series data can be reasonably well explained using a self-consistent dynamic melting model. Klein and Langmuir (1987) and Bourdon et al. (1996a) predicted a long melt column beneath the ridge that generates large degree melts and, thus, thick crust and shallow axial depths, and our modeling efforts support these basic predictions. Such a melt column likely would originate well within the garnet stability field, which is capable of producing the observed ^{230}Th and ^{231}Pa excesses.

By considering the role of eclogite in the melt region, we also considered hypotheses of Niu and Batiza (1997) and Russo et al. (2009) and, among others, who suggested that secondary mantle lithologies and other variations in the melt regime, besides mantle temperature, can play an important role. We conclude that alternate lithologies such as eclogite may play a minor role in melt generation, and perhaps a more significant role for samples erupted along the isotopically enriched Eggvin Bank ridge segment.

Long-lived isotopic and trace element data, particularly Sm/Nd and $^{143}Nd/^{144}Nd$ ratios, indicate that the mantle source for the majority of Kolbeinsey Ridge lavas has most likely experienced a depletion event considerably more recently than typical 1.8 Ga mantle ages. As shown schematically in Fig. 11, our measurements and calculations thus overall suggest that the mantle source for Kolbeinsey Ridge basalts begins melting deep in a long, mostly peridotitic melt column, and that it is relatively depleted and young in age relative to the decay of ^{147}Sm to ^{143}Nd.

6. CONCLUSIONS

MORB from the slow-spreading Kolbeinsey Ridge form a nearly horizontal trend on a plot of $(^{230}Th/^{232}Th)$ vs. $(^{238}U/^{232}Th)$. Correlation of $(^{230}Th/^{238}U)$ with $(^{234}U/^{238}U)$ suggests that ^{238}U excess ($(^{230}Th/^{238}U) < 1$) samples reflect shallow crustal alteration in the presence of seawater or seawater-derived shallow crustal materials. Thus it would appear that unaltered Kolbeinsey MORB have universally high ^{230}Th excesses.

Trace element ratios and concentrations are generally depleted in Kolbeinsey MORB, reflecting a depleted mantle source beneath the ridge axis. Most Kolbeinsey basalts also have $\alpha_{Sm-Nd} > 1$, which favors a relatively young source, as previously suggested by Salters (1996).

The high $(^{230}Th/^{238}U)$ and $(^{231}Pa/^{235}U)$ values measured along most of the Kolbeinsey Ridge are consistent with dynamic melting of a slowly-upwelling, peridotitic mantle source. The thick Kolbeinsey crust and major element systematics indicate large degrees of melting and, therefore, a deep onset of melting. These observations are consistent with a first-order, global mantle temperature control on ^{238}U–^{230}Th isotope systematics, as suggested by Bourdon et al. (1996a). On the other hand, the low $(^{231}Pa/^{235}U)$ ratio of a sample from the isotopically enriched Eggvin Bank suggests that eclogite may play a role in the source for that ridge segment, reflecting local variations in source lithologies.

ACKNOWLEDGMENTS

This work has benefited from thoughtful and insightful reviews by V. Salters, A. Pietruszka, and an anonymous reviewer, and from valuable conversations and interactions with a number of colleagues: Rob Sohn, Stan Hart, Peter Kelemen, Fred Frey, Glenn Gaetani, Marc Speigelman, Susan Humphris, and Chris Waters. This research was funded by NSF OCE-0422278 to K.W.W.S. and NSF OCE-1061037/1060434 to L.J.E. and K.W.W.S. J.B.T. acknowledges financial support from the French Institut National des Sciences de l'Univers.

APPENDIX A. SUPPLEMENTARY DATA

Supplementary data associated with this article can be found, in the online version, at doi:10.1016/j.gca.2011.08.020.

REFERENCES

Andres M., Blichert-Toft J. and Schilling J. G. (2004) Nature of the depleted upper mantle beneath the Atlantic: evidence from Hf isotopes in normal mid-ocean ridge basalts from 79°N to 55°S. *Earth Planet. Sci. Lett.* **225**, 89–103.

Aumento F. (1971) Uranium content of mid-ocean ridge basalts. *Earth Planet. Sci. Lett.* **11**, 90–94.

Bacon M. P. (1978) Radioactive disequilibrium in altered mid-oceanic basalts. *Earth Planet. Sci. Lett.* **39**, 250–254.

Ball L., Sims K. W. W. and Schwieters J. (2008) Measurement of U-234/U-238 and Th-230/Th-232 in volcanic rocks using the Neptune MC–ICP-MS. *J. Anal. Atom. Spectrom.* **23**, 173–180.

Bauch H. A., Erlenkeuser H., Spielhagen R. F., Struck U., Matthiessen J., Thiede J. and Heinemeier J. (2001) A multiproxy reconstruction of the evolution of deep and surface waters in the subarctic Nordic seas over the last 30,000 yr. *Quater. Sci. Rev.* **20**, 659–678.

Baumann K. H., Lackschewitz K. S., Erlenkeuser H., Henrich R. and Junger B. (1993) Late quaternary calcium-carbonate sedimentation and terrigenous input along the east Greenland continental-margin. *Mar. Geol.* **114**, 13–36.

Beattie P. (1993a) The generation of uranium series disequilibria by partial melting of spinel peridotite: constraints from partitioning studies. *Earth Planet. Sci. Lett.* **117**, 379–391.

Beattie P. (1993b) Uranium thorium disequilibria and partitioning on melting of garnet peridotite. *Nature* **363**, 63–65.

Blichert-Toft J. (2001) On the Lu–Hf isotope geochemistry of silicate rocks. *Geostand. Newsl. – J. Geostand. Geoanal.* **25**, 41–56.

Blichert-Toft J., Chauvel C. and Albarède F. (1997) Separation of Hf and Lu for high-precision isotope analysis of rock samples by magnetic sector-multiple collector ICP-MS. *Contrib. Mineral. Petrol.* **127**, 248–260.

Blichert-Toft J., Agranier A., Andres M., Kingsley R., Schilling J. G. and Albarede F. (2005) Geochemical segmentation of the Mid-Atlantic Ridge north of Iceland and ridge-hot spot interaction in the North Atlantic. *Geochem. Geophys. Geosyst.* **6**, Q01E19.

Bourdon B., Zindler A., Elliott T. and Langmuir C. H. (1996a) Constraints on mantle melting at mid-ocean ridges from global U-238–Th-230 disequilibrium data. *Nature* **384**, 231–235.

Bourdon B., Langmuir C. H. and Zindler A. (1996b) Ridge-hotspot interaction along the Mid-Atlantic Ridge between 37°30′ and 40°30′N: the U–Th disequilibrium evidence. *Earth Planet. Sci. Lett.* **142**, 175–189.

Bourdon B., Joron J. L., Claude-Ivanaj C. and Allegre C. J. (1998) U–Th–Pa–Ra systematics for the Grande Comore volcanics: melting processes in an upwelling plume. *Earth Planet. Sci. Lett.* **164**, 119–133.

Bourdon B., Goldstein S. J., Bourles D., Murrell M. T. and Langmuir C. H. (2000) Evidence from 10Be and U series disequilibria on the possible contamination of mid-ocean ridge basalt glasses by sedimentary material. *Geochem. Geophys. Geosyst.* **1**, 2000GC000047.

Bourdon B., Turner S. P. and Ribe N. M. (2005) Partial melting and upwelling rates beneath the Azores from a U-series isotope perspective. *Earth Planet. Sci. Lett.* **239**, 42–56.

Brandsdottir B., Richter B., Riedel C., Dahm T., Helgadottir G., Kjartansson E., Detrick R., Magnusson A., Asgrimsson A. L., Palsson B. H., Karson J., Saemundsson K., Mayer L. A., Calder B. and Driscoll N.W. (2004). Tectonic details of the Tjornes fracture zone, an onshore–offshore ridge-transform in N-Iceland. *Eos Trans. American Geophys.* Union 85, Abstract T41A-1172.

Breivik A. J., Faleide J. I., Mjelde R. and Flueh E. R. (2009) Magma productivity and early seafloor spreading rate correlation on the northern Voring Margin, Norway: constraints on mantle melting. *Tectonophysics* **468**, 206–223.

Carroll M. R. and Webster J. D. (1994) Solubilities of sulfur, noble gases, nitrogen, chlorine, and fluorine in magmas. In *Reviews in Mineralogy: Volatiles in Magmas* (eds. M. R. Carroll and J. R. Holloway). Mineralogical Society of America, Fredericksburg, VA.

Charette M. A., Moore W. S. and Burnett W. C. (2008) Uranium- and thorium-series nuclides as tracers of submarine groundwater discharge. *Radioact. Environ. U–Th Ser. Nuclides Aquat. Syst.* **13**, 155–191.

Chauvel C. and Blichert-Toft J. (2001) A hafnium isotope and trace element perspective on melting of the depleted mantle. *Earth Planet. Sci. Lett.* **190**, 137–151.

Chen J. H., Wasserburg G. J., von Damm K. L. and Edmond J. M. (1986) The U–Th–Pb systematics in hot springs on the East Pacific rise at 21°N and Guaymas Basin. *Geochim. Cosmochim. Acta* **50**, 2467–2479.

Cheng H., Edwards R. L., Hoff J., Gallup C. D., Richards D. A. and Asmerom Y. (2000) The half-lives of uranium-234 and thorium-230. *Chem. Geol.* **169**, 17–33.

Claude-Ivanaj C., Bourdon B. and Allegre C. J. (1998) Ra–Th–Sr isotope systematics in Grande Comore Island: a case study of plume–lithosphere interaction. *Earth Planet. Sci. Lett.* **164**, 99–117.

Claude-Ivanaj C., Joron J. L. and Allegre C. J. (2001) U-238–Th-230–Ra-226 fractionation in historical lavas from the Azores: long-lived source heterogeneity vs. metasomatism fingerprints. *Chem. Geol.* **176**, 295–310.

Cohen R. S., Evensen N. M., Hamilton P. J. and Onions R. K. (1980) U–Pb, Sm–Nd and Rb–Sr systematics of mid-ocean ridge basalt glasses. *Nature* **283**, 149–153.

Condomines M., Morand P., Allegre C. J. and Sigvaldason G. (1981) Th-230–U-238 disequilibria in historical lavas from Iceland. *Earth Planet. Sci. Lett.* **55**, 393–406.

Condomines M. and Sigmarsson O. (2000) U-238–Th-230 disequilibria and mantle melting processes: a discussion. *Chem. Geol.* **162**, 95–104.

Coombs M. L., Sisson T. W. and Kimura J. I. (2004) Ultra-high chlorine in submarine Kilauea glasses: evidence for direct assimilation of brine by magma. *Earth Planet. Sci. Lett.* **217**, 297–313.

Cooper K. M., Goldstein S. J., Sims K. W. W. and Murrell M. T. (2003) Uranium-series chronology of Gorda Ridge volcanism: new evidence from the 1996 eruption. *Earth Planet. Sci. Lett.* **206**, 459–475.

Debaille V., Trønnes R. G., Brandon A. D., Waight T. E. and Graham D. W. (2009) Primitive off-rift basalts from Iceland and Jan Mayen: Os-isotopic evidence for a mantle source containing enriched subcontinental lithosphere. *Geochim. Cosmochim. Acta* **73**, 3423–3449.

DePaolo D. (1988) *Neodymium Isotope Geochemistry: An Introduction*. Springer, 187 pp.

Devey C. W., Garbeschonberg C. D., Stoffers P., Chauvel C. and Mertz D. F. (1994) Geochemical effects of dynamic melting beneath ridges: reconciling major and trace-element variations in Kolbeinsey (and global) Midocean Ridge basalt. *J. Geophys. Res. – Solid Earth* **99**, 9077–9095.

Donnelly K. E., Goldstein S. L., Langmuir C. H. and Spiegelman M. (2004) Origin of enriched ocean ridge basalts and implications for mantle dynamics. *Earth Planet. Sci. Lett.* **226**, 347–366.

Dupre B. and Allegre C. J. (1980) Pb–Sr–Nd isotopic correlation and the chemistry of the North-Atlantic mantle. *Nature* **286**, 17–22.

Elkins L. J., Gaetani G. A. and Sims K. W. W. (2008) Partitioning of U and Th during garnet pyroxenite partial melting: constraints on the source of alkaline ocean island basalts. *Earth Planet. Sci. Lett.* **265**, 270–286.

Elliott T. (1997) Fractionation of U and Th during mantle melting: a reprise. *Chem. Geol.* **139**, 165–183.

Faure G. and Mensing T. M. (2005) *Isotopes: Principles and Applications*, third ed. John Wiley and Sons, Inc., Hoboken, New Jersey.

Fjeldskaar W., Grunnaleite I., Zweigel J., Mjelde R., Faleide J. I. and Wilson J. (2009) Modelled palaeo-temperature on Voring, offshore mid-Norway: the effect of the lower crustal body. *Tectonophysics* **474**, 544–558.

Frujiter C., Elliott T. and Schlager W. (2000) Mass-spectrometric ^{234}U–^{230}Th ages from the Key Largo Formation, Florida Keys, United States: constraints on diagenetic age disturbance. *Geol. Soc. Am. Bull.* **112**, 267–277.

Furman T., Frey F. A. and Park K. H. (1991) Chemical constraints on the petrogenesis of mildly alkaline lavas from Vestmannaeyjar, Iceland: the Eldfell (1973) and Surtsey (1963–1967) eruptions. *Contrib. Mineral. Petrol.* **109**, 19–37.

Gill J., Torssander P., Lapierre H., Taylor R. N., Kaiho K., Koyama M., Kusakabe M., Aitchison J., Cisowski S., Dadey

K., Fujioka K., Klaus A., Lovell M., Marsaglia K., Pezard P., Taylor B. and Tazaki K. (1990) Explosive deep-water basalt in the Sumisu Backarc Rift. *Science* **248**, 1214–1217.

Glass J. B., Cooper K. M., Alt J. C., Elliott T. and Teagle D. A. (2005) Recent Alteration of 15-Ma Oceanic Crust, ODP Site 1256, Leg 206. *Eos. Trans. Am. Geophys. Union* **86**, V43B–1568.

Goldstein S. J., Murrell M. T. and Jackecky D. R. (1989) Th and U isotopic systematics of basalts from the Juan de Fuca and Gorda ridges by mass spectrometry. *Earth Planet. Sci. Lett.* **96**, 134–146.

Goldstein S. J., Murrell M. T., Janecky D. R., Delaney J. R. and Clague D. A. (1992) Geochronology and petrogenesis of Morb from the Juan-De-Fuca and Gorda ridges by U-238 Th-230 disequilibrium. *Earth Planet. Sci. Lett.* **109**, 255–272.

Goldstein S. J., Murrell M. T. and Williams R. W. (1993) Pa-231 and Th-230 chronology of Midocean Ridge basalts. *Earth Planet. Sci. Lett.* **115**, 151–159.

Green D. H., Falloon T. J., Eggins S. M. and Yaxley G. M. (2001) Primary magmas and mantle temperatures. *Eur. J. Mineral.* **13**, 437–451.

Haase K. M., Devey C. W. and Wieneke M. (2003) Magmatic processes and mantle heterogeneity beneath the slow-spreading northern Kolbeinsey Ridge segment, North Atlantic. *Contrib. Mineral. Petrol.* **144**, 428–448.

Hanan B. B., Blichert-Toft J., Kingsley R. and Schilling J. G. (2000) Depleted Iceland mantle plume geochemical signature: artifact of multicomponent mixing? *Geochem. Geophys. Geosyst.* **1**, 1003.

Hardarson B. S. and Fitton J. G. (1997) Mechanisms of crustal accretion in Iceland. *Geology* **25**, 1043–1046.

Hards V. L., Kempton P. D. and Thompson R. N. (1995) The heterogeneous Iceland plume: new insights from the alkaline basalts of the Snaefell volcanic center. *J. Geol. Soc. London* **152**, 1003–1009.

Hart S. R. and Blusztajn J. (2006) Age and geochemistry of the mafic sills, ODP site 1276, Newfoundland margin. *Chem. Geol.* **235**, 222–237.

Hart S. R., Hauri E. H., Oschmann L. A. and Whitehead J. A. (1992) Mantle plumes and entrainment: isotopic evidence. *Science* **256**, 517–520.

Hauri E. H., Wagner T. P. and Grove T. L. (1994) Experimental and natural partitioning of Th, U, Pb and other trace-elements between garnet, clinopyroxene and basaltic melts. *Chem. Geol.* **117**, 149–166.

Hemond C., Arndt N. T., Lichtenstein U., Hofmann A. W., Oskarsson N. and Steinthorsson S. (1993) The heterogeneous Iceland plume: Nd–Sr–O isotopes and trace-element constraints. *J. Geophys. Res. – Solid Earth* **98**, 15833–15850.

Henderson G. M., Cohen A. S. and Onions R. K. (1993) U-234/U-238 ratios and Th-230 ages for Hateruma Atoll corals: implications for coral diagenesis and seawater U-234/U-238 ratios. *Earth Planet. Sci. Lett.* **115**, 65–73.

Hilton D. R., Thirlwall M. F., Taylor R. N., Murton B. J. and Nichols A. (2000) Controls on magmatic degassing along the Reykjanes Ridge with implications for the helium paradox. *Earth Planet. Sci. Lett.* **183**, 43–50.

Hirschmann M. M. and Stolper E. M. (1996) A possible role for garnet pyroxenite in the origin of the "garnet signature" in MORB. *Contrib. Mineral. Petrol.* **124**, 185–208.

Hoffmann D. L., Prytulak J., Richards D. A., Elliott T., Coath C. D., Smart P. L. and Scholz D. (2007) Procedures for accurate U and Th isotope measurements by high precision MC–ICPMS. *Int. J. Mass Spectrom.* **264**, 97–109.

Hoffmann D. L., Richards D. A., Elliott T. R., Smart P. L., Coath C. D. and Hawkesworth C. J. (2005) Characterisation of secondary electron multiplier nonlinearity using MC–ICPMS. *Int. J. Mass Spectrom.* **244**, 97–108.

Hofmann A. W. (1988) Chemical differentiation of the Earth: the relationship between mantle, continental crust, and oceanic crust. *Earth Planet. Sci. Lett.* **90**, 297–314.

Hooft E. E. E., Brandsdóttir B., Mjelde R., Shimamura H. and Murai Y. (2006) Asymmetric plume–ridge interaction around Iceland: the Kolbeinsey Ridge Iceland seismic experiment. *Geochem. Geophys. Geosyst.* **7**, Q05015.

Iwamori H. (1994) 238U–230Th–226Ra and 235U–231Pa disequilibria produced by mantle melting with porous and channel flows. *Earth Planet. Sci. Lett.* **125**, 1–16.

Jackson M. G. and Hart S. R. (2006) Strontium isotopes in melt inclusions from Samoan basalts: implications for heterogeneity in the Samoan plume. *Earth Planet. Sci. Lett.* **245**, 260–277.

Jaffey A. H., Flynn K. F., Glendeni Le, Bentley W. C. and Essling A. M. (1971) Precision measurement of half-lives and specific activities of U-235 and U-238. *Phys. Rev. C* **4**, 1889–1906.

Jakobsson M., Macnab R., Mayer L., Anderson R., Edwards M., Hatzky J., Schenke H. W. and Johnson P. (2008) An improved bathymetric portrayal of the Arctic Ocean: implications for ocean modeling and geological, geophysical and oceanographic analyses. *Geophys. Res. Lett.* **35**, L07602–L07605.

Jull M., Kelemen P. and Sims K. (2002) Consequences of diffuse and channeled porous melt migration on uranium series disequilibria. *Geochim. Cosmochim. Acta* **66**, A719.

Kelemen P. B., Hirth G., Shimizu N., Spiegelman M. and Dick H. J. B. (1997) A review of melt migration processes in the adiabatically upwelling mantle beneath oceanic spreading ridges. *Philos. Trans. R. Soc. London Ser. a – Math. Phys. Eng. Sci.* **355**, 283–318.

Klein E. M. and Langmuir C. H. (1987) Global correlations of ocean ridge basalt chemistry with axial depth and crustal thickness. *J. Geophys. Res. – Solid Earth* **92**, 8089–8115.

Knudsen K. L., Jiang H., Jansen E., Eiriksson J., Heinemeier J. and Seidenkrantz M. S. (2004) Environmental changes off North Iceland during the deglaciation and the Holocene: foraminifera, diatoms and stable isotopes. *Marine Micropaleontol.* **50**, 273–305.

Kodaira S., Mjelde R., Gunnarsson K., Shiobara H. and Shimamura H. (1997) Crustal structure of the Kolbeinsey Ridge, North Atlantic, obtained by use of ocean bottom seismographs. *J. Geophys. Res. – Sol Earth* **102**, 3131–3151.

Kogiso T., Hirschmann M. M. and Pertermann M. (2004) High-pressure partial melting of mafic lithologies in the mantle. *J. Petrol.* **45**, 2407–2422.

Kokfelt T. F., Hoernle K. and Hauff F. (2003) Upwelling and melting of the Iceland plume from radial variation of U-238–Th-230 disequilibria in postglacial volcanic rocks. *Earth Planet. Sci. Lett.* **214**, 167–186.

Kokfelt T. F., Lundstrom C., Hoernle K., Hauff F. and Werner R. (2005) Plume–ridge interaction studied at the Galapagos spreading center: evidence from Ra-226–Th-230–U-238 and Pa-231–U-235 isotopic disequilibria. *Earth Planet. Sci. Lett.* **234**, 165–187.

Koornneef J. M., Stracke A., Aciego S., Reubi O. and Bourdon B. (2010) A new method for U–Th–Pa–Ra separation and accurate measurement of U-234–Th-230–Pa-231–Ra-226 disequilibria in volcanic rocks by MC–ICPMS. *Chem. Geol.* **277**, 30–41.

Krolikowska-Ciaglo S., Deyhle A., Hauff F. and Hoernle K. (2007) Boron isotope geochemistry and U–Pb systematics of altered MORB from the Australian Antarctic Discordance (ODP Leg 187). *Chem. Geol.* **242**, 458–472.

Ku T. L., Knauss K. G. and Mathieu G. G. (1977) Uranium in open ocean: concentration and isotopic composition. *Deep-Sea Res.* **24**, 1005–1017.

La Tourette T. Z. and Burnett D. S. (1992) Experimental determination of U-partitioning and Th-partitioning between cpx and natural and synthetic basaltic liquid. *Earth Planet. Sci. Lett.* **110**, 227–244.

La Tourette T. Z., Kennedy A. K. and Wasserburg G. J. (1993) Thorium–uranium fractionation by garnet: evidence for a deep source and rapid rise of oceanic basalts. *Science* **261**, 729–742.

Lackschewitz K. S., Wallrabeadams H. J. and Garbeschonberg D. (1994) Geochemistry of surface sediments from the Midoceanic Kolbeinsey Ridge, North of Iceland. *Mar. Geol.* **121**, 105–119.

Landwehr D., Blundy J., Chamorro-Perez E. M., Hill E. and Wood B. (2001) U-series disequilibria generated by partial melting of spinel lherzolite. *Earth Planet. Sci. Lett.* **188**, 329–348.

Langmuir C., Klein E. M. and Plank T. (1992) Petrological systematics of mid-ocean ridge basalts: constraints on melt generation beneath ocean ridges. In *Mantle Flow and Melt Generation at Mid-Ocean Ridges*. AGU Geophysical Monograph, pp. 183–280.

Le Roux L. J. and Glendenin L. E. (1963). Half-life of ^{232}Th. In *Proceedings of the National Meeting on Nuclear Energy, Pretoria, South Africa*, pp. 83–94.

le Roex P. J., Shirey S. B., Hauri E. H., Perfit M. R. and Bender J. F. (2006) The effects of variable sources, processes and contaminants on the composition of northern EPR MORB (8–10°N and 12–14°N): evidence from volatiles (H_2O, CO_2, S) and halogens (F, Cl). *Earth Planet. Sci. Lett.* **251**, 209–231.

Ludwig K. A., Shen C.-C., Kelley D., Cheng H. and Edwards R. L. (2011) U–Th systematics and ^{230}Th ages of carbonate chimneys at the Lost City hydrothermal field. *Geochim. Cosmochim. Acta* **75**, 1869–1888.

Lundstrom C. (2000) Models of U-series disequilibria generation in MORB: the effects of two scales of melt porosity. *Phys. Earth Planet. Inter.* **121**, 189–204.

Lundstrom C. C. (2003) Uranium-series disequilibria in mid-ocean ridge basalts: observations and models of basalt genesis. *Rev. Mineral. Geochem.* **52**, 175–214.

Lundstrom C. C., Shaw H. F., Ryerson F. J., Phinney D. L., Gill J. B. and Williams Q. (1994) Compositional controls on the partitioning of U, Th, Ba, Pb, Sr and Zr between clinopyroxene and haplobasaltic melts: implications for uranium series disequilibria in basalts. *Earth Planet. Sci. Lett.* **128**, 407–423.

Lundstrom C. C., Gill J., Williams Q. and Perfit M. R. (1995) Mantle melting and basalt extraction by equilibrium porous flow. *Science* **270**, 1958–1961.

Lundstrom C. C., Gill J., Williams Q. and Hanan B. B. (1998a) Investigating solid mantle upwelling beneath mid-ocean ridges using U-series disequilibria. II. A local study at 33° Mid-Atlantic Ridge. *Earth Planet. Sci. Lett.* **157**, 167–181.

Lundstrom C. C., Williams Q. and Gill J. B. (1998b) Investigating solid mantle upwelling rates beneath mid-ocean ridges using U-series disequilibria, 1: a global approach. *Earth Planet. Sci. Lett.* **157**, 151–165.

Lundstrom C. C., Sampson D. E., Perfit M. R., Gill J. and Williams Q. (1999) Insights into mid-ocean ridge basalt petrogenesis: U-series disequilibria from the Siqueiros Transform, Lamont Seamounts, and East Pacific Rise. *J. Geophys. Res. – Solid Earth* **104**, 13035–13048.

Macdougall J. D. (1977) Uranium in marine basalts: concentration, distribution and implications. *Earth Planet. Sci. Lett.* **35**, 65–70.

Macdougall J. D., Finkel R. C., Carlson J. and Krishnaswami S. (1979) Isotopic evidence for uranium exchange during low-temperature alteration of oceanic basalt. *Earth Planet. Sci. Lett.* **42**, 27–34.

Mckenzie D. (1985) Th-230–U-238 disequilibrium and the melting processes beneath ridge axes. *Earth Planet. Sci. Lett.* **72**, 149–157.

Mertz D. F., Devey C. W., Todt W., Stoffers P. and Hofmann A. W. (1991) Sr–Nd–Pb isotope evidence against plume asthenosphere mixing north of Iceland. *Earth Planet. Sci. Lett.* **107**, 243–255.

Mertz D. F. and Haase K. M. (1997) The radiogenic isotope composition of the high-latitude North Atlantic mantle. *Geology* **25**, 411–414.

Mertz D. F., Sharp W. D. and Haase K. M. (2004) Volcanism on the Eggvin Bank (Central Norwegian-Greenland Sea, latitude similar to 71°N): age, source, and relationship to the Iceland and putative Jan Mayen plumes. *J. Geodyn.* **38**, 57–83.

Michael P. (1995) Regionally distinctive sources of depleted MORB: evidence from trace-elements and H_2O. *Earth Planet. Sci. Lett.* **131**, 301–320.

Michael P. J., Chase R. L. and Allan J. F. (1989) Petrologic and geologic variations along the southern explorer ridge, Northeast Pacific-Ocean. *J. Geophys. Res. – Solid Earth* **94**, 13895–13918.

Michael P. J. and Cornell W. C. (1998) Influence of spreading rate and magma supply on crystallization and assimilation beneath mid-ocean ridges: evidence from chlorine and major element chemistry of mid-ocean ridge basalts. *J. Geophys. Res. – Solid Earth* **103**, 18325–18356.

Michard A. and Albarede F. (1985) Hydrothermal uranium uptake at ridge crests. *Nature* **317**, 244–246.

Michard A., Albarède F., Michard G., Minster J. F. and Charlou J. L. (1983) Rare-earth elements and uranium in high-temperature solutions from East Pacific Rise hydrothermal vent field (13°N). *Nature* **303**, 795–797.

Mitchell N. (1993) A model for attenuation of backscatter due to sediment accumulations and its application to determine sediment thicknesses with GLORIA sidescan sonar. *J. Geophys. Res. – Solid Earth* **98**, 22477–22493.

Mjelde R., Raum T., Breivik A. J. and Faleide J. I. (2008) Crustal transect across the North Atlantic. *Mar. Geophys. Res.* **29**, 73–87.

Mjelde R., Raum T., Kandilarov A., Murai Y. and Takanami T. (2009) Crustal structure and evolution of the outer More Margin, NE Atlantic. *Tectonophysics* **468**, 224–243.

Montesi L. G. J. and Behn M. D. (2007) Mantle flow and melting underneath oblique and ultraslow mid-ocean ridges. *Geophys. Res. Lett.* **34**, L24307.

Moran S. B., Shen C. C., Weinstein S. E., Hettinger L. H., Hoff J. H., Edmonds H. N. and Edwards R. L. (2001) Constraints on deep water age and particle flux in the Equatorial and South Atlantic Ocean based on seawater Pa-231 and Th-230 data. *Geophys. Res. Lett.* **28**, 3437–3440.

Mosar J., Lewis G. and Torsvik T. H. (2002) North Atlantic sea-floor spreading rates: implications for the Tertiary development of inversion structures of the Norwegian-Greenland Sea. *J. Geol. Soc. London* **159**, 503–515.

Moune S., Sigmarsson O., Thordarson T. and Gauthier P. J. (2007) Recent volatile evolution in the magmatic system of Hekla volcano, Iceland. *Earth Planet. Sci. Lett.* **255**, 373–389.

Murton B. J., Taylor R. N. and Thirlwall M. F. (2002) Plume–ridge interaction: a geochemical perspective from the Reykjanes Ridge. *J. Petrol.* **43**, 1987–2012.

Neumann E. R. and Schilling J. G. (1984) Petrology of basalts from the Mohns–Knipovich Ridge: the Norwegian-Greenland sea. *Contrib. Mineral. Petrol.* **85**, 209–223.

Niu Y. L. and Batiza R. (1993) Chemical variation trends at fast and slow-spreading Midocean ridges. *J. Geophys. Res. – Solid Earth* **98**, 7887–7902.

Niu Y. L. and Batiza R. (1997) Trace element evidence from seamounts for recycled oceanic crust in the eastern Pacific mantle. *Earth Planet. Sci. Lett.* **148**, 471–483.

Niu Y. L., Bideau D., Hekinian R. and Batiza R. (2001) Mantle compositional control on the extent of mantle melting, crust production, gravity anomaly, ridge morphology, and ridge segmentation: a case study at the Mid-Atlantic Ridge 33–35°N. *Earth Planet. Sci. Lett.* **186**, 383–399.

O'Nions R. K. and Pankhurst R. J. (1973) Secular variation in Sr-isotope composition of Icelandic volcanic-rocks. *Earth Planet. Sci. Lett.* **21**, 13–21.

Peate D. W., Hawkesworth C. J., van Calsteren P. W., Taylor R. N. and Murton B. J. (2001) U-238–Th-230 constraints on mantle upwelling and plume–ridge interaction along the Reykjanes Ridge. *Earth Planet. Sci. Lett.* **187**, 259–272.

Pelt E., Chabaux F., Innocent C., Navarre-Sitchler A. K., Sak P. B. and Brantley S. L. (2008) Uranium–thorium chronometry of weathering rinds: rock alteration rate and paleo-isotopic record of weathering fluids. *Earth Planet. Sci. Lett.* **276**, 98–105.

Pertermann M. and Hirschmann M. (2003). Partial melting experiments on MORB-like pyroxenite between 2 and 3 GPa: constraints on the presence of pyroxenite in basalt source regions from solidus location and melting rate. *J. Geophys. Res.* **108**(B2), 2125.

Pertermann M., Hirschmann M. M., Hametner K., Gunther D. and Schmidt M. W. (2004) Experimental determination of trace element partitioning between garnet and silica-rich liquid during anhydrous partial melting of MORB-like eclogite. *Geochem. Geophys. Geosyst.* **5**, Q05A01.

Pickett D. A. and Murrell M. T. (1997) Observations of (^{231}Pa)/(^{235}U) disequilibrium in volcanic rocks. *Earth Planet. Sci. Lett.* **148**, 259–271.

Pietruszka A. J., Hauri E. H. and Blichert-Toft J. (2009) Crustal contamination of mantle-derived magmas within Piton de la Fournaise Volcano, Réunion Island. *J. Petrol.* **50**, 661–684.

Pietruszka A. J., Keyes M. J., Duncan J. A., Hauri E. H., Carlson R. W. and Garcia M. O. (2011) Excesses of seawater-derived 234U in volcanic glasses from Loihi Seamount due to crustal contamination. *Earth Planet. Sci. Lett.* **304**, 280–289.

Pietruszka A. J., Rubin K. H. and Garcia M. O. (2001) Ra-226–Th-230–U-238 disequilibria of historical Kilauea lavas (1790–1982) and the dynamics of mantle melting within the Hawaiian plume. *Earth Planet. Sci. Lett.* **186**, 15–31.

Poreda R., Schilling J. G. and Craig H. (1986) Helium and hydrogen isotopes in ocean-ridge basalts north and south of Iceland. *Earth Planet. Sci. Lett.* **78**, 1–17.

Prytulak J. and Elliott T. (2009) Determining melt productivity of mantle sources from U-238–Th-230 and U-235–Pa-231 disequilibria; an example from Pico Island, Azores. *Geochim. Cosmochim. Acta* **73**, 2103–2122.

Prytulak J., Elliott T., Hoffmann D. L. and Coath C. D. (2008) Assessment of USGS BCR-2 as a reference material for silicate rock u-pa disequilibrium measurements. *Geostand. Geoanal. Res.* **32**, 55–63.

Ravizza G., Blusztajn J., Von Damm K. L., Bray A. M., Bach W. and Hart S. R. (2001) Sr isotope variations in vent fluids from 9 degrees 46′−9°54′N East Pacific rise: evidence of a non-zero-Mg fluid component. *Geochim. Cosmochim. Acta* **65**, 729–739.

Regelous M., Turner S. P., Elliott T. R., Rostami K. and Hawkesworth C. J. (2004) Measurement of femtogram quantities of protactinium in silicate rock samples by multicollector inductively coupled plasma mass spectrometry. *Anal. Chem.* **76**, 3584–3589.

Richter S. Alonso A. Truyens J. Kühn H. Verbruggen A. and Wellum R. (2006). REIMEP 18: inter-laboratory comparison for the measurement of uranium isotopic radios in nitric acid solution. European Commission.

Robert J., Miranda C. F. and Muxart R. (1969) Mesure de la periode du protactinium-231 par microcalorimetrie. *Radiochim. Acta* **11**, 104–108.

Robinson L. F., Henderson G. M., Hall L. and Matthews I. (2004) Climatic control of riverine and seawater uranium-isotope ratios. *Science* **305**, 851–854.

Rubin K. H. (2001) Analysis of Th-232/Th-230 in volcanic rocks: a comparison of thermal ionization mass spectrometry and other methodologies. *Chem. Geol.* **175**, 723–750.

Rubin K. H., van der Zander I., Smith M. C. and Bergmanis E. C. (2005) Minimum speed limit for ocean ridge magmatism from Pb-210–Ra-226–Th-230 disequilibria. *Nature* **437**, 534–538.

Russo C. J., Rubin K. H. and Graham D. W. (2009) Mantle melting and magma supply to the Southeast Indian Ridge: the roles of lithology and melting conditions from U-series disequilibria. *Earth Planet. Sci. Lett.* **278**, 55–66.

Salters V. J. M. (1996) The generation of mid-ocean ridge basalts from the Hf and Nd isotope perspective. *Earth Planet. Sci. Lett.* **141**, 109–123.

Salters V. J. M. and Hart S. R. (1989) The Hafnium paradox and the role of garnet in the source of Mid-Ocean-ridge basalts. *Nature* **342**, 420–422.

Salters V. J. M. and Longhi J. (1999) Trace element partitioning during the initial stages of melting beneath mid-ocean ridges. *Earth Planet. Sci. Lett.* **166**, 15–30.

Salters V. J. M., Longhi J. E. and Bizimis M. (2002) Near mantle solidus trace element partitioning at pressures up to 3.4 GPa. *Geochem. Geophys. Geosyst.* **3**, 1038.

Salters V. J. M. and White W. M. (1998) Hf isotope constraints on mantle evolution. *Chem. Geol.* **145**, 447–460.

Schilling J. G. (1975) Rare-Earth variations across normal-segments of Reykjanes Ridge, 60–53°N, Mid-Atlantic Ridge, 29°S, and East Pacific rise, 2–19°S, and evidence on composition of underlying low-velocity layer. *J. Geophys. Res.* **80**, 1459–1473.

Schilling J. G., Kingsley R., Fontignie D., Poreda R. and Xue S. (1999) Dispersion of the Jan Mayen and Iceland mantle plumes in the Arctic: a He–Pb–Nd–Sr isotope tracer study of basalts from the Kolbeinsey, Mohns, and Knipovich ridges. *J. Geophys. Res. – Solid Earth* **104**, 10543–10569.

Schilling J. G., Zajac M., Evans R., Johnston T., White W., Devine J. D. and Kingsley R. (1983) Petrologic and geochemical variations along the Mid-Atlantic ridge from 29°N to 73°N. *Am. J. Sci.* **283**, 510–586.

Shen Y. and Forsyth D. W. (1995) Geochemical constraints on initial and final depths of melting beneath Midocean ridges. *J. Geophys. Res. – Solid Earth* **100**, 2211–2237.

Sigmarsson O., Carn S. and Carracedo J. C. (1998) Systematics of U-series nuclides in primitive lavas from the 1730–36 eruption on Lanzarote, Canary Islands, and implications for the role of garnet pyroxenites during oceanic basalt formations. *Earth Planet. Sci. Lett.* **162**, 137–151.

Sigurdsson H. (1981) 1st-order major element variation in basalt glasses from the Mid-Atlantic Ridge: 29°N to 73°N. *J. Geophys. Res.* **86**, 9483–9502.

Sims K. W. W. and Hart S. R. (2006) Comparison of Th, Sr, Nd and Pb isotopes in oceanic basalts: implications for mantle heterogeneity and magma genesis. *Earth Planet. Sci. Lett.* **245**, 743–761.

Sims K. W. W., Depaolo D. J., Murrell M. T., Baldridge W. S., Goldstein S. J. and Clague D. A. (1995) Mechanisms of magma generation beneath Hawaii and Midocean ridges – uranium/thorium and samarium/neodymium isotopic evidence. *Science* **267**, 508–512.

Sims K. W. W., DePaolo D. J., Murrell M. T., Baldridge W. S., Goldstein S., Clague D. and Jull M. (1999) Porosity of the melting zone and variations in the solid mantle upwelling rate beneath Hawaii: Inferences from U-238–Th-230–Ra-226 and U-235–Pa-231 disequilibria. *Geochim. Cosmochim. Acta* **63**, 4119–4138.

Sims K. W. W., Goldstein S. J., Blichert-Toft J., Perfit M. R., Kelemen P., Fornari D. J., Michael P., Murrell M. T., Hart S. R., DePaolo D. J., Layne G., Ball L., Jull M. and Bender J. (2002) Chemical and isotopic constraints on the generation and transport of magma beneath the East Pacific Rise. *Geochim. Cosmochim. Acta* **66**, 3481–3504.

Sims K. W. W., Blichert-Toft J., Fornari D. J., Perfit M. R., Goldstein S. J., Johnson P., DePaolo D. J., Hart S. R., Murrell P. J., Michael P. J., Layne G. D. and Ball L. A. (2003) Aberrant youth: chemical and isotopic constraints on the origin of off-axis lavas from the East Pacific Rise, 9–10°N. *Geochem. Geophys. Geosyst.* **4**, 8621.

Sims K. W. W., Perfit M., Blichert-Toft J., Fornari D., Blusztajn J., Ball L. and Waters C. L. (2006) Progressive melting of a heterogeneous mantle source beneath 9–10°N EPR. *Geochim. Cosmochim. Acta* **70**, A592.

Sims K. W. W., Gill J. B., Dosseto A., Hoffmann D. L., Lundstrom C. C., Williams R. W., Ball L., Tollstrup D., Turner S., Prytulak J., Glessner J. J. G., Standish J. J. and Elliott T. (2008a) An inter-laboratory assessment of the thorium isotopic composition of synthetic and rock reference materials. *Geostand. Geoanal. Res.* **32**, 65–91.

Sims K. W. W., Hart S. R., Reagan M. K., Blusztajn J., Staudigel H., Sohn R. A., Layne G. D. and Ball L. A. (2008b) ^{238}U–^{230}Th–^{226}Ra–^{210}Pb–^{210}Po, ^{232}Th–^{228}Ra, and ^{235}U–^{231}Pa constraints on the ages and petrogenesis of Vailulu'u and Malumalu lavas, Samoa. *Geochem. Geophys. Geosyst.* **9**, Q04003.

Smith W. H. F. and Sandwell D. T. (1997) Global sea floor topography from satellite altimetry and ship depth soundings. *Science* **277**, 1956–1962.

Sohn R. A. (2005) A general inversion for end-member ratios in binary mixing systems. *Geochem. Geophys. Geosyst.* **6**, Q11007.

Soule S. A., Fornari D. J., Perfit M. R., Ridley W. I., Reed M. H. and Cann J. R. (2006) Incorporation of seawater into mid-ocean ridge lava flows during emplacement. *Earth Planet. Sci. Lett.* **252**, 289–307.

Soule S. A., Fornari D. J., Perfit M. R. and Rubin K. H. (2007) New insights into mid-ocean ridge volcanic processes from the 2005–2006 eruption of the East Pacific Rise, 9°46′N–9°56′N. *Geology* **1079**, 1082.

Spiegelman M. (2000) UserCalc: a web-based uranium series calculator for magma migration problems. *Geochem. Geophys. Geosyst.* **1**, 1016.

Spiegelman M. and Elliott T. (1993) Consequences of melt transport for uranium series disequilibrium in young lavas. *Earth Planet. Sci. Lett.* **118**, 1–20.

Standish J. J. and Sims K. W. W. (2010) Young off-axis volcanism along the ultraslow-spreading Southwest Indian Ridge. *Nat. Geosci.* **3**, 286–292.

Staudigel H., Davies G. R., Hart S. R., Marchant K. M. and Smith B. M. (1995) Large scale isotopic Sr, Nd and O isotopic anatomy of altered oceanic crust: DSDP/ODP sites 417/418. *Earth Planet. Sci. Lett.* **130**, 169–185.

Stecher O., Carlson R. W. and Gunnarsson B. (1999) Torfajokull: a radiogenic end-member of the Iceland Pb-isotopic array. *Earth Planet. Sci. Lett.* **165**, 117–127.

Störzer D. and Selo M. (1976) Uranium contents and fission track ages of some basalts from the FAMOUS area. *Bull. Soc. Geol. France* **18**, 807–810.

Störzer D. and Selo M. (1978) Chrono-thermometry by fission-track methods of basalts from Legs 51–52 and some aspects of the alteration of these rocks by sea water. *Bull. Soc. Geol. France* **20**, 250–253.

Stracke A., Bourdon B. and McKenzie D. (2006) Melt extraction in the Earth's mantle: constraints from U–Th–Pa–Ra studies in oceanic basalts. *Earth Planet. Sci. Lett.* **244**, 97–112.

Stracke A., Zindler A., Salters V. J. M., McKenzie D., Blichert-Toft J., Albarede F. and Gronvold K. (2003a) Theistareykir revisited. *Geochem. Geophys. Geosyst.* **4**, 8507.

Stracke A., Zindler A., Salters V. J. M., McKenzie D. and Gronvold K. (2003b) The dynamics of melting beneath Theistareykir, northern Iceland. *Geochem. Geophys. Geosyst.* **4**, 8513.

Stroncik N. A. and Schmincke H. U. (2002) Palagonite: a review. *Int. J. Earth Sci.* **91**, 680–697.

Sturm M. E., Goldstein S. J., Klein E. M., Karson J. A. and Murrell M. T. (2000) Uranium-series age constraints on lavas from the axial valley of the Mid-Atlantic Ridge, MARK area. *Earth Planet. Sci. Lett.* **181**, 61–70.

Sun S. S. and Jahn B. (1975) Lead and strontium isotopes in postglacial basalts from Iceland. *Nature* **255**, 527–530.

Tepley F. J., Lundstrom C. C., Sims K. W. W. and Hekinian R. (2004) U-series disequilibria in MORB from the Garrett Transform and implications for mantle melting. *Earth Planet. Sci. Lett.* **223**, 79–97.

Thirlwall M. F., Gee M. A. M., Taylor R. N. and Murton B. J. (2004) Mantle components in Iceland and adjacent ridges investigated using double-spike Pb isotope ratios. *Geochim. Cosmochim. Acta* **68**, 361–386.

Thurber D. (1962) Anomalous ^{234}U/^{238}U in nature. *J. Geophys. Res.* **67**, 4518–4520.

Todt W., Cliff R. A., Hanser A. and Hofmann A. (1996) Evaluation of a ^{202}Pb-^{205}Pb double spike for high-precision lead isotope analysis. In *Earth Processes Reading the Isotope Code* (eds. A. Basu and S. R. Hart). AGU, pp. 429–437.

Tronnes R. G., Planke S., Sundvoll B. and Imsland P. (1999) Recent volcanic rocks from Jan Mayen: low-degree melt fractions of enriched northeast Atlantic mantle. *J. Geophys. Res. – Solid Earth* **104**, 7153–7168.

Turekian K. K. and Bertine K. K. (1971) Deposition of molybdenum and uranium along major Ocean Ridge systems. *Nature* **229**, 250–251.

Turner S., Hawkesworth C., Rogers N. and King P. (1997) U-Th isotope disequilibria and ocean island basalt generation in the Azores. *Chem. Geol.* **139**, 145–164.

Verma S. P. (1992) Seawater alteration effects on REE, K, Rb, Cs, Sr, U, Th, Pb and Sr–Nd–Pb isotope systematics of Mid-Ocean Ridge basalt. *Geochem. J.* **26**, 159–177.

Waggoner D. (1989) *An Isotopic and Trace Element Study of Mantle Heterogeneity Beneath the Norwegian-Greenland Sea*. University of Rhode Island, Kingston, RI, p. 270.

Waters C. L., Sims K. W. W., Perfit M. R., Blichert-Toft J. and Blusztajn J. (2011) Perspective on the genesis of E-MORB from chemical and isotopic heterogeneity at 9–10°N East Pacific rise. *J. Petrol.* **52**, 565–602.

Widom E., Carlson R. W., Gill J. B. and Schmincke H. U. (1997) Th–Sr–Nd–Pb isotope and trace element evidence for the origin of the Sao Miguel, Azores, enriched mantle source. *Chem. Geol.* **140**, 49–68.

Williams R. W. and Gill J. B. (1989) Effects of partial melting on the uranium decay series. *Geochim. Cosmochim. Acta* **53**, 1607–1619.

Wood B. J., Blundy J. D. and Robinson J. A. C. (1999) The role of clinopyroxene in generating U-series disequilibrium during mantle melting. *Geochim. Cosmochim. Acta* **63**, 1613–1620.

Workman R. K. and Hart S. R. (2005) Major and trace element composition of the depleted MORB mantle (DMM). *Earth Planet. Sci. Lett.* **231**, 53–72.

Zou H. B. (1998) Trace element fractionation during modal and nonmodal dynamic melting and open-system melting: a mathematical treatment. *Geochim. Cosmochim. Acta* **62**, 1937–1945.

Zou H. B. and Zindler A. (2000) Theoretical studies of U-238–Th-230–Ra-226 and U-235–Pa-231 disequilibria in young lavas produced by mantle melting. *Geochim. Cosmochim. Acta* **64**, 1809–1817.

Zou H. B., Zindler A. and Niu Y. L. (2002) Constraints on melt movement beneath the East Pacific Rise from Th-230–U-238 disequilibrium. *Science* **295**, 107–110.

Associate editor: Richard J. Walker